Microwave Response of Nonlinear Oscillations in Resistively Shunted Superconducting Nanowires

by

Emily Toomey

Submitted to the Department of Electrical Engineering and Computer Science
in partial fulfillment of the requirements for the degree of

Master of Science in Electrical Engineering

at the

MASSACHUSETTS INSTITUTE OF TECHNOLOGY

September 2017

Author . . . .
Department of Electrical Engineering and Computer Science
August 31, 2017

Certified by . . . .
Karl K. Berggren
Professor of Electrical Engineering and Computer Science
Thesis Supervisor

Accepted by . . . .
Leslie A. Kolodziejski
Professor of Electrical Engineering and Computer Science
Chair, Department Committee on Graduate Students

Microwave Response of Nonlinear Oscillations in Resistively Shunted Superconducting Nanowires

by

Emily Toomey

Submitted to the Department of Electrical Engineering and Computer Science
on August 31, 2017, in partial fulfillment of the
requirements for the degree of
Master of Science in Electrical Engineering

Abstract

Many superconducting technologies such as rapid single flux quantum computing (RSFQ) and superconducting quantum interference devices (SQUIDs) rely on the modulation of nonlinear dynamics in Josephson junctions for functionality. More recently, however, superconducting devices have been developed based on the switching and thermal heating of nanowires for use in fields such as single photon detection and digital logic. In this Master's thesis, I will use resistive shunting to control the nonlinear heating of a superconducting nanowire and compare the resulting dynamics to those observed in Josephson junctions. In particular, I will use a microwave drive to modulate the nonlinear behavior of the shunted nanowire, and will relate the observed results to the AC Josephson effect. New nanowire devices based on these conclusions may have promising applications in fields such as parametric amplification and frequency multiplexing.

Thesis Supervisor: Karl K. Berggren
Title: Professor of Electrical Engineering and Computer Science

Acknowledgments

This thesis is not just a representation of my own work, but a testament to the immense support and advice from my colleagues, family, and friends. In particular, I would like to thank:

My advisor, Prof. Karl Berggren, for his intellectual curiosity and belief in my abilities. His openness to exploring new research directions gave me the freedom to investigate problems at the intersection of engineering design and fundamental science.

Qing-Yuan Zhao, for his endless patience and willingness to guide me as I grow as a researcher. Under his mentorship I learned to never give up on my device, and to approach experiments thoughtfully and intentionally.

Adam McCaughan, for being my first mentor in this field and for encouraging me to take risks with my work. His enthusiasm and passion for research continue to inspire me.

Dorothy Fleischer, for her generosity and help with keeping me organized.

Mark Mondol and Jim Daley, for their expertise and support with fabrication. Without their training, I would never have learned the skills necessary to build my devices.

Di Zhu, Andrew Dane, Francesco Bellei, and Brenden Butters for their many helpful discussions, collaborations, and experimental assistance.

Emma Caldwell, Jane Heyes, Sarah Goodman, Neerja Aggarwal, and Ranveig Flatabø for their advice and friendship.

Navid Abedzadeh, for keeping me grounded and laughing through even the most difficult parts of graduate school.

Jenna Norton, for being the best roommate that anyone could ask for and for helping me to keep things in perspective.

My parents and three brothers, who I am thankful for every day. They are my foundation and my biggest source of pride. Thank you for supporting what I do and for reminding me that I am more than just my work.

Contents

List of Figures

List of Tables

Chapter 1

Introduction

1.1 Superconductors: a nonlinear element

Nonlinear dynamics are at the cornerstone of many natural phenomena. For instance, cardiac rhythms [1] and auditory neuron firings [2] have both been described by periodic patterns called relaxation oscillations, which consist of a nonlinear element and a feedback cycle [3]. These models have also been ascribed to physical systems such as the modulated semiconductor laser [4], and have use in technologies such as tone generators [5],[6], clock signals [7], [8],[9], and sensors [10].

Superconductors are an ideal platform for studying such dynamics. In addition to being governed by systems of nonlinear equations dependent on the superconducting phase, the transition from the superconducting to normal state is a nonlinear perturbation in itself. This transition is facilitated by surpassing one of three critical parameters of the superconducting material — the critical magnetic field (H_c), critical temperature (T_c), or critical current density (J_c). As a result, superconductors may be viewed as nonlinear elements that are modulated by experimental parameters, making them prime candidates for the development of oscillatory devices.

1.1.1 Josephson junctions

The unique nonlinear behavior of Josephson junctions (JJs) have made them the most prominent superconducting device for circuit applications. As illustrated in Figure 1-1(a), a basic Josephson junction is comprised of two superconducting layers sandwiching a thin nonsuperconducting (normal or insulating) barrier. In 1962, B.D. Josephson predicted that the paired electrons of a superconductor (Cooper pairs) could tunnel through such a barrier at currents below the critical current, I_c, without developing a resistance; above I_c, the superconducting current would alternate at a frequency of $f = 2eV/h$, where e is the electronic charge, V is the applied voltage, and h is Planck's constant [11]. An applied voltage of 10 μV, for example, would lead to an oscillation of roughly 4.84 GHz.

The Josephson junction is an inherently quantum mechanical device in its reliance on the coherence of the superconducting electrons. Treated as bosons, the paired superconducting electrons can be described by a collective wavefunction $\Psi = \Psi_0 e^{i\phi(r,t)}$, where ϕ is the spatially and temporally dependent phase. As indicated in Fig. 1-1(a), the barrier in a JJ allows for a phase difference ($\Delta\phi = \phi_L - \phi_R$) to be maintained between the superconducting layers when a bias is applied. Josephson determined that the supercurrent I_s across a junction depends nonlinearly on this phase difference as:

$$I_s = I_c \sin \Delta\phi \tag{1.1}$$

Likewise, the voltage across the barrier is also a function of the phase, defined by:

$$\frac{d\Delta\phi}{dt} = \frac{2eV}{\hbar} = \frac{2\pi V}{\Phi_0} \tag{1.2}$$

Integration of Eq.1.2 with respect to time yields the Josephson oscillation frequency $\omega = 2eV/\hbar$, as mentioned above. As a result, the JJ can be considered a nonlinear quantum mechanical oscillator [12].

The simple relations expressed in Eq.1.1 and Eq.1.2 have enabled a vast number of complex JJ-based technologies in fields such as metrology and computing. For

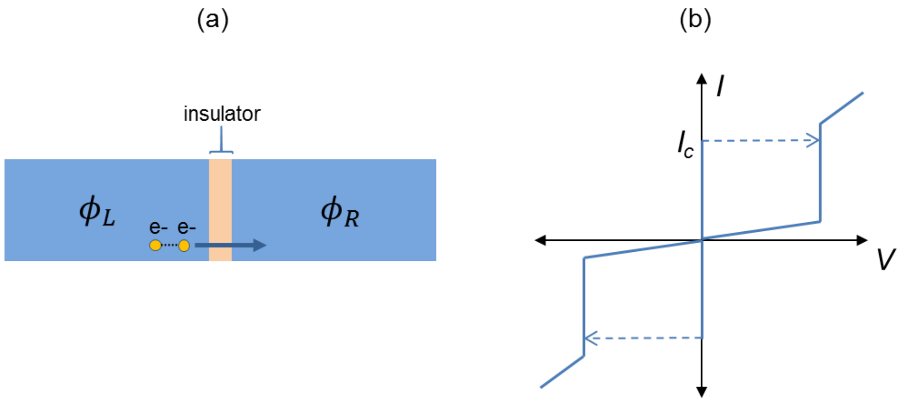

Figure 1-1: (a) Illustration of a Josepshon junction with an insulating barrier showing tunneling of paired superconducting electrons.(b) Typical current-voltage characteristic for a Josephson junction.

instance, the dependence of the oscillation frequency on applied voltage allows JJs to be used as a tool for establishing a voltage standard [13]. The DC SQUID is another example of a JJ based device, comprised of two junctions in parallel. Applying a magnetic field through the superconducting loop modulates the phase of the junctions, which in turn alters their supercurrents. As a result, the SQUID can be used in applications such as magnetic field sensing for biomagnetic imaging [14].

The AC Josephson effect

Originally anticipated in Josephson's first publication on junctions, it was asserted that if AC voltage is superimposed over a DC bias applied to the junction, the supercurrent will have a DC component related to the phase and amplitude of the high frequency signal [11]. This was predicted to form zero slope regions in the DC current-voltage characteristics (IVC) at intervals of $2eV/h = nf$, where f is the frequency of the AC voltage. In 1964 Shapiro et al. experimentally verified these predictions by demonstrating the appearance of zero-slope regions in the IVC at units of $V = nhf/2e$ when junctions were placed in a microwave resonant cavity; consequently, the zero-slope regions are commonly referred to now as "Shapiro steps"[15].

The AC Josephson effect is caused by frequency locking between the high frequency drive and the nonlinear current-phase relationship of the Josephson junction.

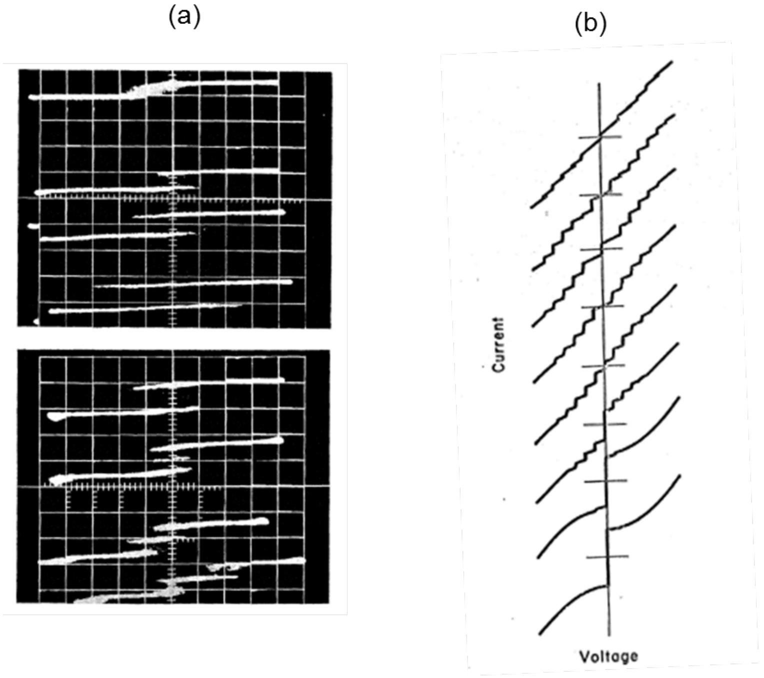

Figure 1-2: The AC Josephon effect. (a) Appearance of steps with microwave radiation reported by Shapiro et al. Figure taken from [15]. (b) Experimental data from [12] of a junction radiated with 24 GHz. Power of the modulation increases from the bottom plot to the top plot.

To see why this is the case, we can examine how the basic relations in Eq.1.1 and Eq.1.2 are changed by a modulated voltage drive, $V(t) = V_0 + V_s cos(\omega_s t)$.

Derivation of the Shapiro voltage

Given that the modulated voltage drive is defined by $V(t) = V_0 + V_s cos(\omega_s t)$, we can solve for the phase of the supercurrent by integrating Eq.1.2:

$$\phi(t) = \int_0^t \frac{2\pi}{\Phi_0} V(t')dt' = \frac{2\pi}{\Phi_0} V_0 t + \frac{2\pi}{\Phi_0 \omega_s} V_s \sin(\omega_s t) + \phi(0) \tag{1.3}$$

Obtaining the phase allows for the calculation of the superconducting current through the current-phase relationship given in Eq.1.1:

$$I_s = I_c \sin\phi(t) = I_c \sin(\frac{2\pi}{\Phi_0} V_0 t + \frac{2\pi}{\Phi_0 \omega_s} V_s \sin(\omega_s t) + \phi(0)) \tag{1.4}$$

Equation 1.4 can be rearranged into the form:

$$I_s = I_c \sin(at + b\sin(\omega_s t) + c) = I_c Im\left\{e^{i(at+b\sin(\omega_s t)+c)}\right\} \tag{1.5}$$

where $a = \frac{2\pi}{\Phi_0}V_0$, $b = \frac{2\pi}{\Phi_0\omega_s}V_s$, and $c = \phi(0)$. This can be further simplified using the Bessel identity $e^{ib\sin x} = \sum_n J_n(b)e^{inx}$ such that the total supercurrent can be written as [16]:

$$I_s = I_c \sum_n (-1)^n J_n(\frac{2\pi}{\Phi_0\omega_s}V_s)\sin(\phi(0) + \frac{2\pi}{\Phi_0}V_0 t - n\omega_s t) \tag{1.6}$$

By examining the sinusoidal term in Equation 1.6, it is clear that the supercurrent only has a lossless DC contribution when the time dependent factors cancel one another so that $n\omega_s t = \frac{2\pi}{\Phi_0}V_0 t$. Thus, at voltage intervals of $V_0 = n\omega_s\Phi_0/2\pi = nhf/2e$ there is only a DC supercurrent of $I_{s,DC} = I_c(-1)^n J_n(\frac{2\pi}{\Phi_0\omega_s}V_s)$. These DC branches in the time-averaged current-voltage characteristics are Shapiro steps.

1.1.2 Superconducting nanowires

While Josephson junctions remain the most widely used superconducting technology, recent devices have been developed based on the switching and thermal heating of superconducting nanowires. Unlike Josephson junctions, superconducting nanowires do not operate through the tunneling of Cooper pairs. Instead, nanowires experience a local breakdown in superconductivity when the temperature, current, or magnetic field exceeds their critical values. The breakdown then creates a normal region of hot quasiparticles in the nanowire known as a hotspot, which can expand to the full length of the nanowire, causing it to latch.

This relatively simple operation principle has enabled many novel devices used in detection and logic. Figure 1-3 highlights three of them. The superconducting nanowire single photon detector (SNSPD) is a planar meandered nanowire device first demonstrated in 2001 by Gol'tsman et al. [17]. In the detection process, the nanowire is current biased slightly below I_c; as a result, when a photon hits and deposits energy, the local temperature T increases and reduces $I_c(T)$ below the bias level. This generates a hotspot that expands across the nanowire through Joule heating. In a typical SNSPD made from a 100 nm wide niobium nitride nanowire, the hotspot resistance will grow to the order of 1-10 kΩ, producing an appreciable voltage pulse that indicates a detection event.

The nanocryotron, or nTron, is a three-terminal nanowire device that also takes advantage of Joule heating to generate large impedances. As shown in Fig.1-3b, the nTron consists of a narrow gate with a choke connected to a wide channel that is biased below its critical current. Applying a gate pulse greater than $I_{c,gate}$ causes Joule heating in the choke that sends hot quasiparticles into the channel. The injected quasiparticles form a high impedance hotspot in the channel, diverting the channel bias out through a load resistor. In this way the nTron may be used as a switch for digital logic, with the state of the current through the load resistor dependent on the gate input. Additionally, the high resistance of the channel hotspot makes the nTron suitable for supporting substantial fanout and driving large impedances on the order of 100 kΩ [18].

Fig.1-3(c) illustrates a third superconducting nanowire device called the yTron. Like the nTron, it is also a three-terminal device reliant on Joule heating; however, the Joule heating is triggered by a phenomenon known as current crowding rather than by the injection of hot quasiparticles [19]. Current crowding occurs when a supercurrent bends around a sharp corner, leading to a higher current density at the inner radius of curvature. The heightened current density can exceed the critical value J_c and form a localized hotspot, causing premature switching at currents below I_c if the normal region spreads across the width of the wire [20]. The yTron takes advantage of this process by manipulating current crowding between two nanowire branches. When the current density is balanced between the branches, supercurrent flows evenly and superconductivity is maintained; however, when current is removed from one branch, the current in the other branch crowds around the corner and forms a resistive hotspot that generates a voltage pulse. Consequently the yTron can be thought of as a NOT gate, and has applications as a circuit element and readout tool.

These examples emphasize the advantages of thermal nanowire based devices. Unlike Josephson junctions, they are fabricated as planar structures on a single superconducting film and can be densely packed due to their nanoscale size. Furthermore, their reliance on Joule heating allows functionality to be dictated through simple geometric effects, like the current crowding of the yTron. The formation of resistive hotspots also makes them suitable for high impedance environments and easily integrated with standard CMOS circuits [21].

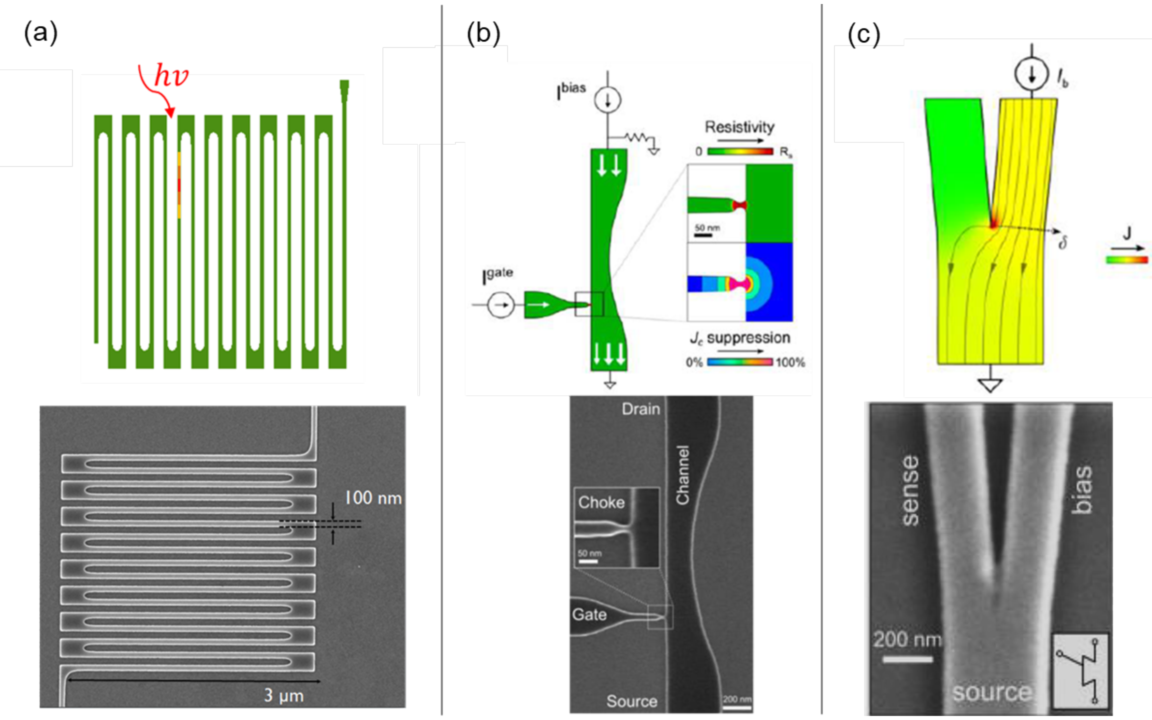

Figure 1-3: Examples of superconducting nanowire devices. (a) Schematic of an SNSPD with a scanning electron micrograph of an actual device with a 100 nm nanowire width. Image courtesy of Di Zhu (MIT). (b) Schematic of the nTron illustrating Joule heating through the injection of a critical current at the gate choke. Scanning electron micrograph of a real device shows a choke dimension of 15 nm and a channel width of 200 nm. Figure adapted from [18].(c) Schematic of the yTron showing Joule heating at the intersection point due to current crowding effects. The scanning electron micrograph shows a real device with an arm width of 200 nm. Figure adapted from [19].

1.2 Motivation: resistive shunting

Despite the advantages offered by a superconducting nanowire's simple operation, dependence on Joule heating limits the overall device performance. In addition to dissipating a considerable amount of power through the creation of a high impedance load, hotspot formation introduces a slow, thermally dependent reset time. SNSPDs of a large active area are usually limited by an inductive electrical decay time on the order of 10 ns [22]; however, the intrinsic recovery time set by the escape of high energy phonons appears to be on the order of 10-100 ps [23],[24]. For thin film niobium nitride, the maximum clock frequency at this limit is estimated to be 1 GHz [18]. Resistive heating also destroys the phase coherence of the superconducting electrons, making the nanowire ineligible for quantum applications where Josephson junctions are typically used.

In recent years, these setbacks have prompted investigations into how the negative impacts of Joule heating can be controlled, suggesting that nanowire-based devices can eventually function in a non-thermal regime. Resistive shunting, commonly used to damp the switching dynamics of Josepshon junctions, is one popular technique for suppressing thermal heating in nanowires [25],[26]. By providing a path to divert the bias current from the nanowire after it switches out of the superconducting state, the shunt resistor limits hotspot growth and allows the nanowire to return to the superconducting state more rapidly, thereby reducing both the reset time and the power dissipated in the device.

The influence of resistive shunting on heating can be observed in the separation between the switching and retrapping currents of the DC current-voltage characteristics, also known as hysteresis. Whereas in Josepshon junctions this separation is predominantly due to capacitance, in nanowires it is a trademark of Joule heating. As noted in Fig. 1-4(a), switching the nanowire leads to a resistive hotspot that continues to increase the local temperature as the bias current is supplied. The nanowire remains in the resistive state until the bias is reduced far below I_{sw} and the hotspot collapses, causing the retrapping current, I_r, to be less than I_{sw} [27],[28]. Shunting has been shown to reduce hysteresis by diverting the bias current away from the hotspot such that Joule heating is reduced, allowing the hotspot to collapse more readily [29].

When taken to an extreme, this result poses an interesting question— is a shunted

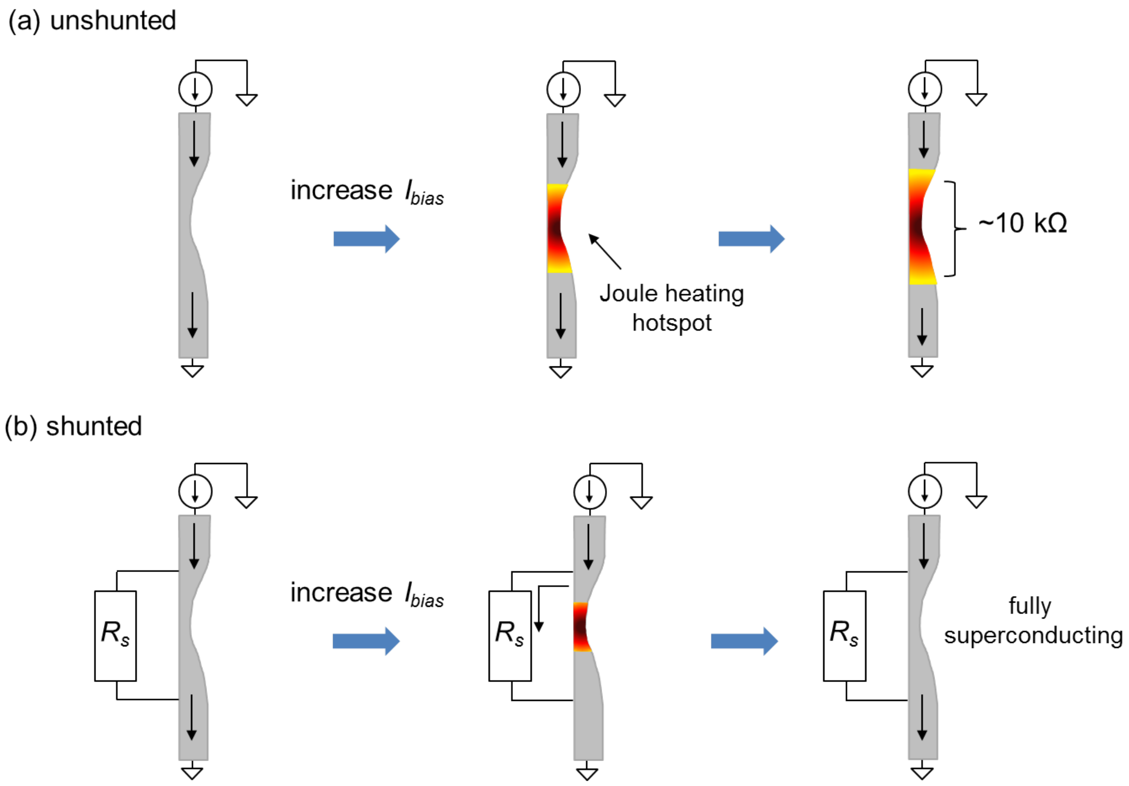

Figure 1-4: Illustration of the diversion of bias current through a resistive shunt. (a) A stable hotspot forms in the unshunted nanowire when the bias current exceeds I_c. (b) Shunting the nanowire allows the bias current to be diverted from the localized hotspot, causing it to collapse more quickly.

nanowire without hysteresis still thermal? Prior work on externally shunted nanowires suggests that critically shunting the nanowire to achieve full suppression of hysteresis leads to a resistive state that is dominated by superconducting phase dynamics rather than Joule heating, thus more closely resembling a Josephson junction [30], [31]. These studies relied solely on DC characterization of the nanowires and used Josephson junction models to match the experimental observations. Conversely, interaction between the hotspot and the impedance of a readout circuit in an SNSPD has been shown to induce relaxation oscillations in which the hotspot periodically forms and collapses [32]. As a result, while both shunting scenarios produce nonlinear dynamics, whether their underlying nature is phase coherent or thermal remains ambiguous.

1.2.1 Thesis goal

The central research goal for this Master's thesis is to study the dynamics of a resistively shunted superconducting nanowire and to evaluate the nature of its nonlinear switching behavior. Initial steps will rely on DC characterization to determine the critical shunt resistance needed for complete suppression of hysteresis, a trademark of reduced thermal heating. High frequency dynamics of the nanowire will also be studied to better understand how they collectively produce the time-averaged DC responses. Further insight will be gained through RF modulation of the nanowire's dynamics; since Josephson junctions are known to produce unique signatures in the presence of microwave radiation, observation of the nanowire's response under similar conditions will help indicate whether a junction based model is appropriate for the shunted nanowire. In addition to electrical measurements, modeling will be needed to understand the observed dynamics and to allow for the design of future shunted devices.

1.2.2 Thesis outline

This thesis will be organized as follows:

Chapter 2— Fabrication and DC characterization. This chapter describes the process for fabricating the superconducting nanowire and designing its shunting circuit. We conducted DC characterization measurements for evaluating the impact of resistive shunting on thermal suppression. The results are analyzed using Josephson junction based models.

Chapter 3—Switching Characteristics. This chapter describes the measurement of high frequency dynamics of the shunted nanowire and introduces a relaxation oscillation model to explain the results. Electrothermal simulations are used to fully characterize the experimentally observed oscillations.

Chapter 4—Microwave Modulation. In this chapter we show that the relaxation oscillations of the shunted nanowire produce similar behavior to the AC Josepshon effect when subject to external microwave radiation. To understand this phenomenon, we study how the high frequency dynamics are modulated by an external drive. A model based on the frequency mixing and locking of a sawtooth waveform to a periodic drive is presented for comparison.

Chapter 5—Conclusions and Future Work. In this chapter we review the central findings presented in this thesis and describe future investigations related to these results.

Chapter 2

Fabrication and DC characterization

This chapter describes the development of the shunted nanowire circuit. We will first discuss fabrication of the nanowire as well as the implementation of an external shunt. In order to assess the degree of thermal suppression caused by shunting, we designed a measurement setup for analyzing the time-averaged current-voltage characteristics. I would like to acknowledge Adam McCaughan for his guidance in teaching me the fabrication process presented in this chapter.

2.1 Nanowire fabrication

A testbed for measuring nanowire characteristics requires two elements: the nanowire itself, and electrical contact pads for probing. In our design, we first patterned gold electrical contact pads that could be connected to the printed circuit board(PCB) through aluminum wirebonds. Following contact patterning, the nanowire was fabricated using electron beam lithography.

2.1.1 Contact pad patterning

NbN film deposition

Prior to patterning, a 40 nm thick niobium nitride (NbN) film was deposited on a 4" wafer (100 nm SiO_2 on n-type Si, (100) orientation) following the procedure described in [33]. This was performed in an AJA sputtering system using Ar and N_2 gas flow. The measured sheet resistance was approximately 59 Ω/square.

It is worth considering why such a thick film was employed. Typical SNSPDs, for example, use NbN films on the order of 4-5 nm thick [34]. There were two principle reasons behind the decision to fabricate on a thicker film. First, the kinetic inductance of a superconducting thin film may be approximated through the expression:

$$L_k = \frac{\hbar R_S}{\pi \Delta_0} \tag{2.1}$$

where R_S is the sheet resistance and Δ_0 is the gap energy following the relationship $\Delta_0 = 1.76 k_B T_c$ according to BCS theory [35]. As a result, it is clear that the inductance varies proportionally to the sheet resistance of the superconducting film. In this circuit, we wanted to minimize the pathway inductance between the nanowire and the resistive shunt in order to reduce the time delay of current diversion to the shunt following hotspot formation. Since the sheet resistance decreases with increasing film thickness, a thicker film will have lower R_S and consequently lower inductance in the bias current path.

Additionally, the nanowires were fabricated on thicker films in order to best reduce damage by electrostatic discharge events (see 2.1.3). As discussed in Chapter 1, superconductors are limited by a critical current density J_c; consequently, the cross-sectional area of a patterned geometry defines a critical current I_c. In restricting ourselves to nanowires with a narrow width of 60 nm, increasing the film thickness enabled us to increase I_c and make the nanowire more robust against damage from static or other sources of extraneous current.

Photolithography

Photolithography with a UV source was used to pattern gold contact pads and electron beam alignment marks. The overall process is outlined as follows:

1. PMGI SF9 was spun onto the wafer at 3 krpm for 60 s, then baked at 90 °C for 60 s. This was to provide a layer to support undercut for metal liftoff.

2. Photoresist S1813 (Shipley Microposit)was spun onto the wafer at 3 krpm for

60 s, then baked at 90 °C for 60 s. S1813 is a positive tone photoresist such that the areas that are exposed during photolithography become more soluble to the developer than the unexposed regions.

3. A contact mask patterned with a laser direct write system (Heidelberg) was used to expose the sample using a contact photolithography system (Tamarack) at 60 mJ/cm^2. This equated to roughly 24 s at 2400 μW/cm^2.

4. The wafer was then developed in the TMAH-based developer CD-26 (Microposit MP, 2.4% TMAH) for 20 s. Development was halted by rinsing the wafer in deionized water for 60 s. Optical microscope examination confirmed that the pattern transfer was successful.

5. Following pattern transfer, a 15 nm titanium adhesion layer and 50 nm of gold were deposited using an electron beam evaporation system.

6. Liftoff of the metal outside of the contact pads was achieved through high power sonication in acetone for 5 min, followed by sonication in CD-26 for 2 min. As before, rinsing in deionized water was used to stop the action of CD-26. Afterwards, optical microscope examination was employed again to confirm successful liftoff.

7. In preparation for packaging, a protective layer of S1813 was spun onto the wafer at 2 krpm. The wafer was then baked at 90 °C for 2 min.

8. The wafer was diced into 1 cm x 1 cm squares, as specified in the mask, using an automatic dicing saw (DAD3240, Disco Corporation).

9. The protective S1813 layer was removed by sonicating individual dies in acetone at high power for 5 min, followed by sonication in IPA at high power for 5 min. The dies were then rinsed in acetone, methanol, and IPA, and dried with a nitrogen gun.

2.1.2 Nanowire patterning

Choice of electron beam resist

Due to the desired width of our nanowire geometry, sub-100 nm resolution was required for fabrication. To date, electrom beam lithography (EBL) is the most widely used technique for achieving structures at this scale. The traditional electron beam resist for ultranarrow resolution is polymethyl methacrylate (PMMA). Conventionally used as a positive tone resist, PMMA is a long, organic polymer chain that is fragmented by electron radiation at low doses, increasing its solubility in a developer solution. While PMMA has been championed for its ability to resolve features on the order of 5 nm, its low etch resistance and pattern instability remain troublesome for reproducible and robust nanofabrication. To compensate for this issue, bilayer liftoff processes have been developed using PMMA in combination with a copolymer PMMA-MMA (PMMA-Methacrylic acid). Unfortunately, this technique is not compatible with refractory metals like niobium, since the high heat of evaporation required by evaporation of refractory metals destabilizes the resist mask, rendering it unusable. Additionally, outgassing from the resist contaminates the metal with oxygen, which drastically changes the critical parameters of the superconducting film [36].

To this end, hydrogen silsesquixane (HSQ) is a newer, alternative resist for fabricating nanoscale devices with superconducting refractory metals. Originally introduced as an interlayer dielectric for integrated circuits, HSQ became a candidate for EBL due to its negative tone behavior under electron radiation. Unlike PMMA, HSQ is a cage-like molecule with eight $(\mathrm{HSiO})_{(3/2)}$ monomers; during exposure, a broken Si-O bond of one molecule links with a broken Si-H bond of a neighboring molecule, forming an Si-O-Si link and hydrogen gas. As a result, exposure converts the porous HSQ cage into a longer network of strong Si-O-Si crosslinks which are insoluble in alkaline hydroxide developers [37].

In addition to HSQ's observed resolution limits on the order of 5 nm, its high etch resistance allows for direct pattern transfer through dry etching without employing a

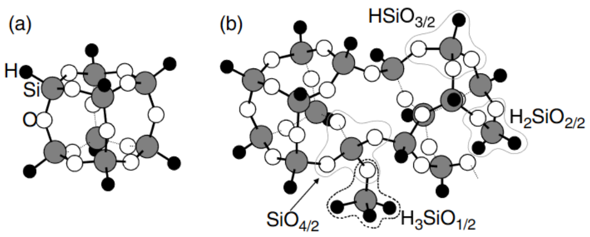

Figure 2-1: Structure of HSQ (a) before radiation; (b) partially cross-linked with intermediate species after radiation.Grey atoms are Si, white atoms are O, and black atoms are H. Figure from [38].

bilayer process, and its small molecular size gives it a minimal line edge roughness. It also has superior electron image contrast to polymer-based resists like PMMA, which often require electron-imaging techniques such as staining or metal coating [37].

Lithographic process

Given the advantages of HSQ for the patterning of refractory metals, it was selected as the electron beam resist for fabricating our NbN nanowires. The overall process is outlined below and illustrated in Figure 2-2.

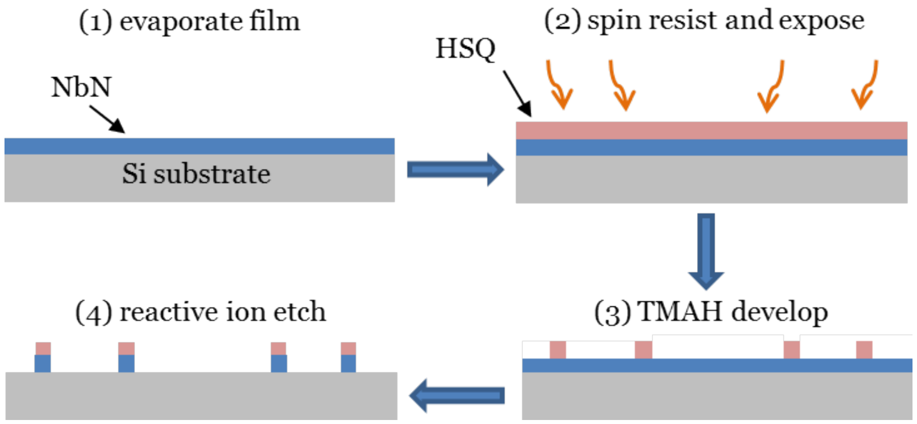

Figure 2-2: Illustration of the main steps in the nanowire pattern transfer using electron beam lithography of HSQ.

1. Prior to spinning resist, the sample (diced to 10 mm x 10 mm) was sonicated in both acetone and IPA at high power for 3 min each. The sample was then dried with a nitrogen gun.

2. After cleaning, the sample was subjected to oxygen plasma ashing at 100 W for

60 s in order to promote HSQ adhesion, as described in 2.1.3 below.

3. During this time, a vial of 6% HSQ was moved out of refrigeration to reach room temperature over a course of approximately 5-10 min.
4. 6% HSQ was then spun onto the sample at 3 krpm for 60 s. The resulting layer was roughly 90 nm thick.
5. The HSQ was patterned using the 125 kV Elionix electron beam lithography system. A 1 nA beam current was used to achieve an areal dose of 3840 μC/cm^2. Alignment was performed manually using the gold marks patterned during the photolithography process.
6. Following exposure, the HSQ was developed in 25% TMAH at room temeprature for 60 s. Development was stopped by rinsing the sample in deionized water for 30 s. The sample was then rinsed in IPA to reduce surface tension, and dried with a nitrogen gun.
7. Pattern transfer was completed using reactive ion etching (PlasmaTherm) in 10 mTorr CF$_4$ at 50 W of RF power for 7 min.

The experiments presented in this thesis relied primarily on four different nanowires fabricated on the same film. The dimensions of each of the nanowires are specified in Table 2.1.

Table 2.1: Dimensions of nanowires under investigation

	Sample A	Sample B	Sample C	Sample D
min width (nm)	60	60	60	200
constriction length (μm)	2	2	2	2
total length (μm)	120	140	180	30
number of squares	100	110	130	42

All nanowires were fabricated on the same die in one lithographic process. The approximate number of squares for each sample was calculated by rounding the result of geometric simulations in COMSOL.

Figure 2-3 shows a scanning electron micrograph of the resulting gold contact pads connected to a nanowire with a minimum width of 60 nm. As detailed in the image, the nanowire was tapered from 2 μm to 60 nm in order to minimize current crowding.

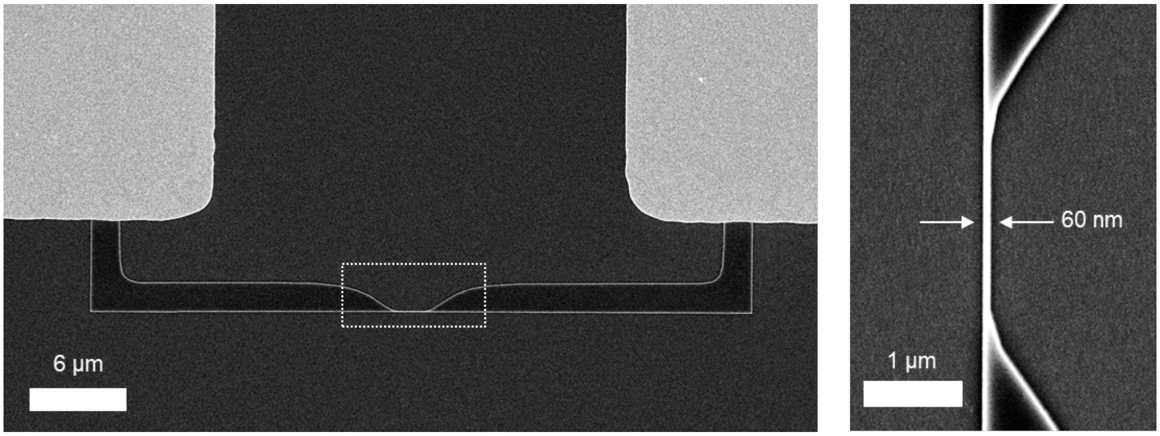

Figure 2-3: (Left) Scanning electron micrograph of a tapered nanowire and gold contact pads. (Right) Enlarged view of the nanowire showing a minimum width of 60 nm.

2.1.3 Fabrication issues

HSQ adhesion

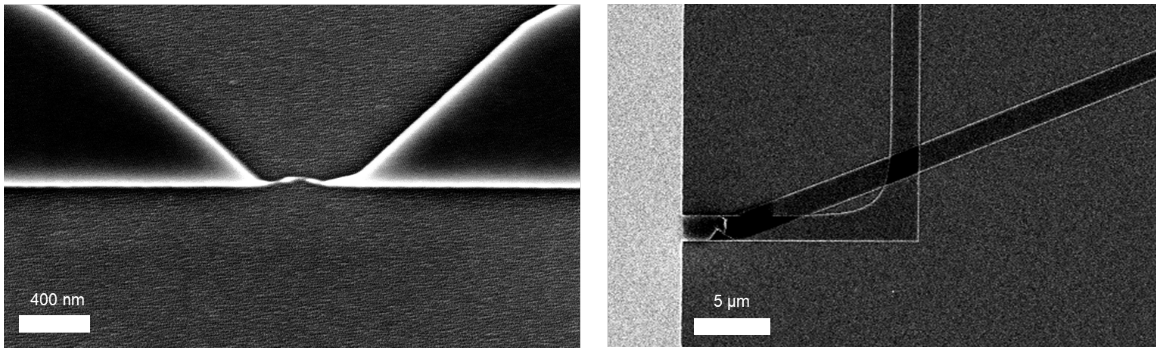

Figure 2-4: Examples of HSQ adhesion problems on NbN films

During the nanowire patterning process, we encountered multiple examples of poor adhesion between the NbN and HSQ. These problems were particularly exacerbated in the narrowest sections of the nanowire, as exhibited in Figure 2-4. While a handful of methods have been proposed to assuage this issue, we chose the technique of subjecting the NbN surface to O_2 plasma ashing. As previously discussed, HSQ reacts by breaking Si-H bonds and forming Si-O-Si links. By activating and oxidizing the surface of the NbN, O_2 plasma ashing takes advantage of the HSQ reaction process and promotes adhesion between the oxide of the surface and the bonds of the HSQ molecules. While this can produce the detrimental side effect of oxidizing the NbN film, our film was quite thick and therefore robust against serious damage from oxidation.

Electrostatic discharge (ESD)

When handling nanowires of sub-100 nm widths, there is a large risk of device damage through electrostatic discharge. Static electricity is present in many packaging environments, and is further supported by fabric fibers, human hair, and other contaminants.

We found that our devices were easily damaged by ESD, wire bonding at high powers, and repetitive room temperature resistance measurements using a digital multimeter. Examples of this damage are shown in the scanning electron micrographs of Figure 2-5. In order to avoid such damage, we determined that several precautions were useful. First, all gold PCB pads were wire bonded to ground prior to bonding to the gold lithographic contact pads attached to the nanowires. Ground bonds were only removed immediately before measurement. Additionally, equipment such as grounding bracelets, ESD shielding boxes for transportation, and conductive tweezers were used for all sample preparation. All ports of the PCB were connected to ground through 50 Ω terminators during the sample transfer into and out of the liquid helium bath.

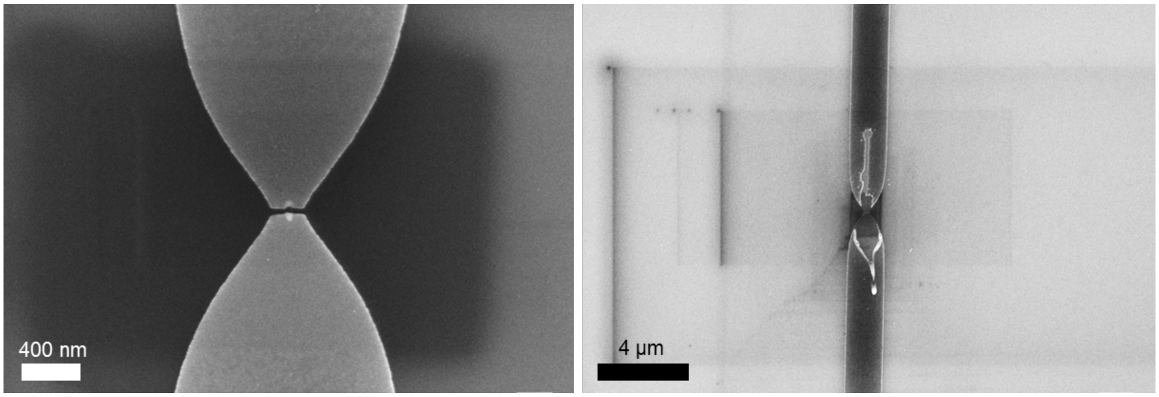

Figure 2-5: Scanning electron micrographs of sample damage through ESD

2.2 DC characterization

DC measurements are useful indicators of the degree of thermal heating in a nanowire. As discussed in Chapter 1, the separation between the switching current and retrapping current, known as hysteresis, is a characteristic of Joule heating after the nanowire transitions into the normal state [28]. By providing a path for the diversion of bias current after the nanowire becomes normal, the shunt resistor limits heating of the nanowire and by relation suppresses hysteresis.

2.2.1 Current-voltage characteristics

External resistive shunting

Prior to measurement, the devices were shunted using external resistors (Vishey Dale Thin Film, gold plated) that could be electrically connected to using aluminum wire bonds. To adhere the resistors to the PCB, a drop of S1813 photoresist was placed on the PCB surface and the resistors were placed on top. The PCB was then left on a hotplate at 70°C for 2 hours, allowing the photoresist to dry. DC characterization of the nanowire was repeated for shunt resistances ranging from 200 Ω to 4.5 Ω in order to find the critical resistance at which no hysteresis was observed.

Low-noise measurement setup

Time-averaged characteristics were obtained using a slow bias current sweep of the nanowire. An Agilent33250a arbitrary waveform generator (AWG) was used to supply a sinusoidal voltage sweep at a frequency of 10 Hz. A series resistor of 10 kΩ was placed between the AWG and the sample. All transport measurements were performed using room temperature electronics connected to the device, which was kept in a liquid helium bath at a temperature of 4.2 K.

Connecting the nanowire in parallel with low shunt resistances proved to greatly reduce the signal voltage output; a shunt of 10 Ω, for instance, reduced the voltage output by three orders of magnitude in comparison to that of the unshunted nanowire. As a result, the signal was much more susceptible to noise. To ameliorate this problem, we soldered 1 kΩ resistors directly onto the PCB in series with all of the ports as a means of dissipating noise in the cryogenic environment. Additionally, we measured the voltage output using a four-point technique. This was facilitated by connecting either end of the nanowire voltage output to the two input ports of an SR560 preamplifier (Stanford Research Systems). The voltage output was taken to be the differential of the two inputs, thereby reducing the ground noise. Furthermore, 1.9 MHz lowpass filters were placed in series with the inputs to the preamplifier. The gain of the preamplifier varied from 10-5000 depending on the magnitude of voltage output from the shunted nanowire.

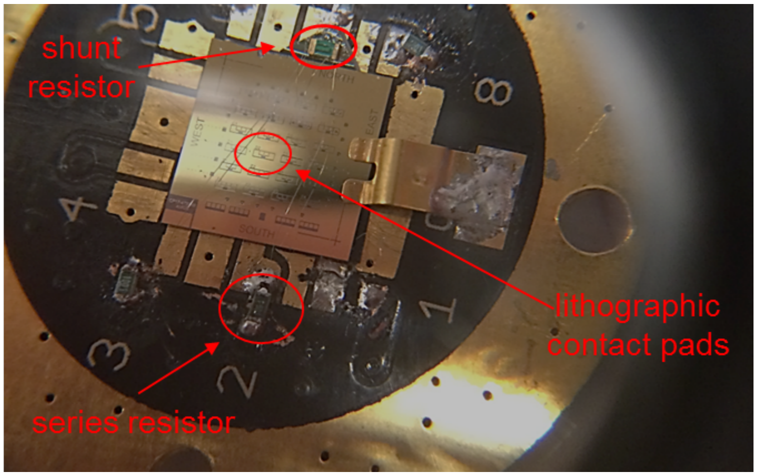

Figure 2-6: Photograph of the PCB with a 10 Ω shunt resistor and 1 kΩ series resistors on all ports.

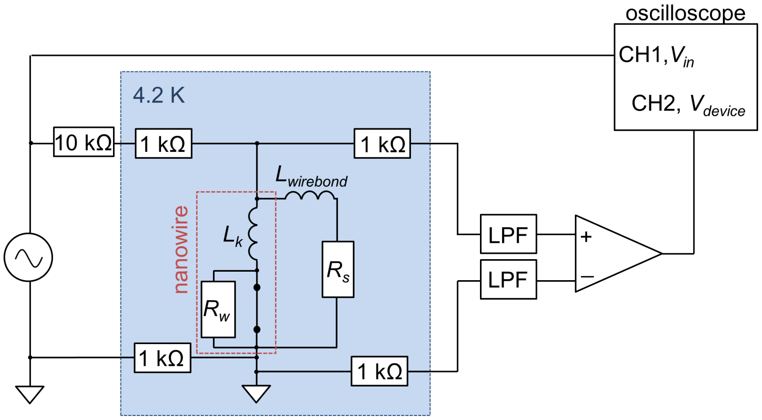

Figure 2-7: Experimental setup for measuring current-voltage characteristics of the nanowire.

Data was collected by connecting the current bias input and the preamplifier's differential voltage output to the channels of a Lecroy 6209Zi oscilloscope (2 GHz, 1 MΩ DC coupling) using SMA cables. Custom Python scripts were used to collect the waveforms and automate the measurement processes by interfacing with the instruments. Data was processed in Matlab.

Results

Figure 2-8 shows the current-voltage characteristics (IVCs) for a 60 nm wide nanowire without a resistive shunt. As indicated by the separation between the switching current and the retrapping current, there is substantial thermal heating in the sample, leading to a hotspot resistance on the order of 10 kΩ.

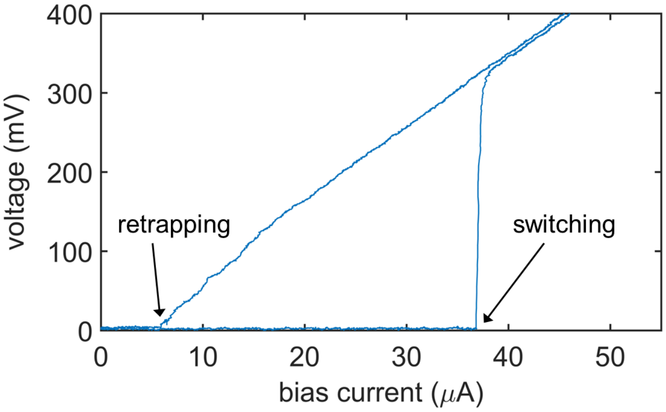

Figure 2-8: Current-voltage characteristics of a 60 nm wide nanowire (Sample B) without a resistive shunt.

In contrast, shunting the nanowire with 10 Ω led to a complete suppression of hysteresis, as indicated in Figure 2-9. Unlike the unshunted IVC, that of the shunted sample has a curved switching transition and a maximum resistance limited by the 10 Ω shunt. The non-hysteretic, curved appearance of the shunted IVC is similar to that of an overdamped Josephson junction in which the contribution of capacitance can be neglected. A fit to the time-averaged voltage as a function of bias current can be made through the expression:

$$\langle V \rangle_{DC} = I_c R \sqrt{I_{bias}/I_c^2 - 1} \tag{2.2}$$

where I_c is the critical current of the junction, R is the total parallel resistance, and

I_{bias} is the current being supplied [16]. The red curve in Figure 2-9 indicates that there is good qualitative agreement between the experimental IVC and the overdamped junction model when the nanowire is shunted with 10 Ω and when the model resistance is set equal to 7.8 Ω. The slight discrepancy is not surprising, however, since the total parallel resistance $R_T = (1/R_{wire} + 1/R_s)^{-1}$ is only expected to reach the full value of R_s when the self-heating hotspot resistance (R_{wire}) has grown to the order of kΩ. Other simplifications in the model including a lack of noise and capacitance terms may also contribute to this deviation. Nonetheless, the qualitative agreement suggests a relationship between the shunted nanowire and an overdamped Josephson junction approximation.

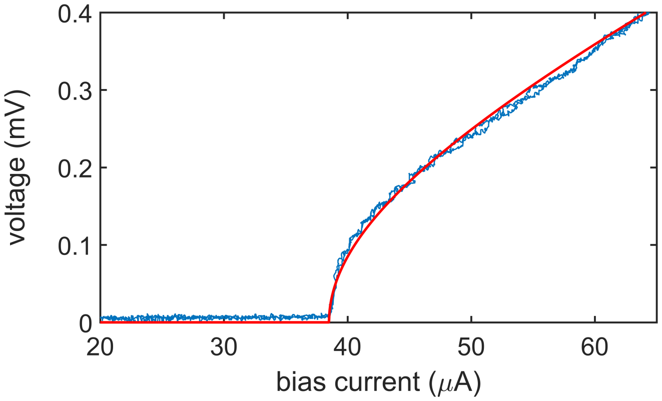

Figure 2-9: Current-voltage characteristics of a 60 nm wide nanowire (Sample B) shunted with 10 Ω. The red curve is a fit to the overdamped Josephson junction model in Eq. 2.2 with $I_c = 38.5\ \mu A$ and $R = 7.8\ \Omega$.

It is important to note that, in addition to suppressing hysteresis, resistive shunting decreases power dissipation in the device. Figure 2-10 shows the calculated power dissipation in a 200 nm wide nanowire with different values of external shunt resistance (plotted as conductance, or $1/R_s$). Power was calculated from the experimental DC current-voltage characteristics at the switching and retrapping points through the simplified approximation $P = I_{wire}V$, where $I_{wire} = I_{bias} - V/R_s$. At a shunt resistance of 4.5 Ω, hysteresis was fully suppressed and the switching power was decreased by three orders of magnitude in comparison to the unshunted nanowire.

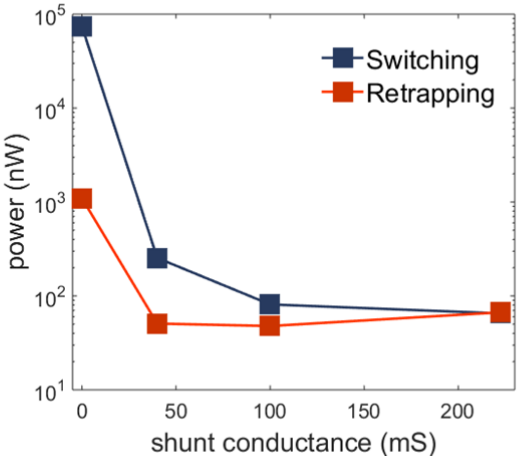

Figure 2-10: Power dissipated in a 200 nm wide NbN nanowire (Sample D, $I_{sw} = 280\ \mu$A) with varying amounts of shunt conductance.

2.2.2 Switching current distribution

The tilted washboard model

In the case of a Josephson junction, switching dynamics reflect its susceptibility to thermal or quantum fluctuations. The simple tilted washboard potential model is often used to visualize this behavior.

The phase evolution of a Josephson junction can be written through the normalized expression:

$$Q_0^2 \frac{d^2\phi}{d\tau^2} + \frac{d\phi}{d\tau} + \sin\phi = i + i_n \tag{2.3}$$

where ϕ is the phase of the junction, $Q_0 = \sqrt{2eI_0R^2C/\hbar}$, and i and i_n are the normalized bias current and current noise expressed as I_{bias}/I_c and I_{noise}/I_c, respectively [30]. The time variable τ is also normalized as $\tau = t(\frac{\hbar}{2eI_cR})^{-1}$. Since Eq. 2.3 describes the time evolution of the phase, it becomes apparent that the variable Q_0^2 can be thought of as inversely proportional to the damping of the phase evolution.

The tilted washboard model uses this interpretation to describe the phase as a particle rolling down a potential described by:

$$U(\phi) = -(i\phi + \cos\phi) \tag{2.4}$$

The first term in the potential describes the linear tilt provided by the bias current, while the second term is the sinusoidal modulation due to the nonlinearity of the junction. As described in Chapter 1, the Josephson relations require that $V = (h/2e)d\phi/dt$; consequently, movement of the particle down the washboard potential indicates a change in phase $d\phi/dt$ and therefore a nonzero voltage. Conversely, when the phase particle is trapped in a local minima of the potential, the average phase velocity is negligible and the material is fully superconducting ($\langle V \rangle \propto \langle d\phi/dt \rangle = 0$). The damping of the phase particle will dictate the ease with which the it moves down the potential and enters the running voltage state.

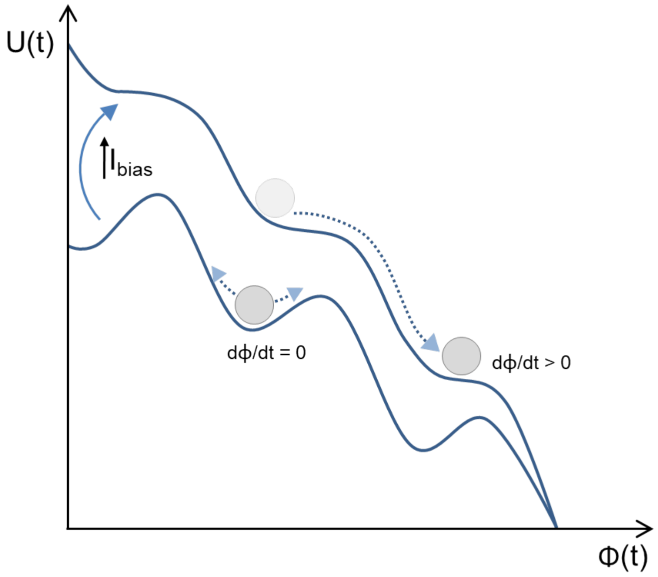

Figure 2-11: Illustration of tilted washboard potential with increasing applied bias current. At low applied bias, the phase particle remains in a local minima and the average velocity is zero. At a higher applied bias, the phase particle can enter the running voltage state, and a finite resistance is formed.

When the junction is underdamped ($Q > 1$), the particle can move down the potential more easily. This implies that the running voltage or resistive state can occur for currents less than I_c (lower tilts on the washboard), so the mean switching current will be lower than I_c and the distribution will have a wide spread. Premature switching at lower bias currents can be triggered by factors such as noise or thermal fluctuations.

Conversely, when the junction is overdamped ($Q << 1$), the phase particle becomes easily trapped in a local minima. As a result, a larger tilt (current bias) is required to move the particle down the potential and create a resistive state. In critically damped cases, the mean of the switching distribution will approach I_c and the distribution will become narrower as the phase particle is less likely to enter the running voltage state due to a single thermal fluctuation.

A Matlab script that generates a graphical user interface for tuning the resistance and bias current of a phase particle in the tilted washboard model may be found in A.0.1 and A.0.2.

Results

The tilted washboard model may aid in interpreting the switching dynamics of the resistively shunted nanowire. Switching distributions were obtained using the same measurement setup as shown in Fig. 2-7; however, the frequency was increased to 200 Hz, corresponding to a slew rate of roughly 0.13 μA/μs. To capture the bias current at which switching occurred, the oscilloscope was triggered on the voltage output of the device (Channel 2 of the oscilloscope) at the level corresponding to a switching voltage jump. The bias current (Channel 1 of the oscilloscope) at this corresponding time was collected. 10,000 counts were collected for each data set. Figure 2-12 compares the switching distributions for the 60 nm wide nanowire with and without the presence of a 10 Ω external shunt. As shown in the figure, adding a resistive shunt led to both an increase in the mean and a narrowing of the width of the switching distribution. Furthermore, the shape of the distribution was changed from a left skewed distribution to a normal distribution. From the perspective of the tilted washboard model, these results may be interpreted as products of changing the damping of the system. Since decreasing R decreases the value of Q_0^2, placing a low resistance shunt in parallel with the nanowire will increase the overall damping of the circuit in comparison to the unshunted device. As a result, the shunted nanowire is less likely to enter the running voltage state from a single thermal or noise fluctuation; rather, it may remain trapped in one of the local minima of the potential until the applied bias current is increased to the true switching current, at which point the

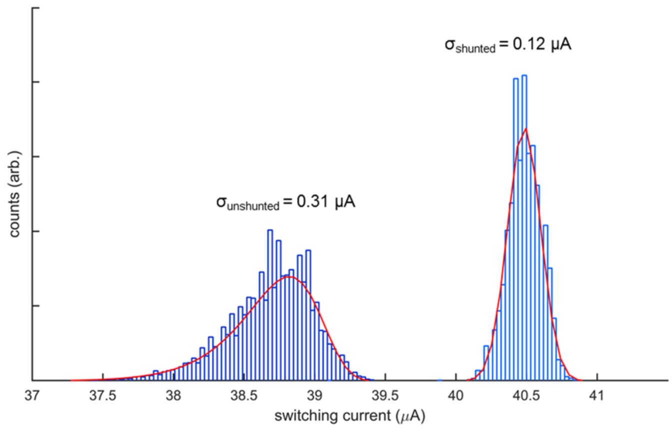

Figure 2-12: Switching current distributions for the unshunted nanowire (Sample B) and the nanowire shunted with 10 Ω.

nanowire will switch into the normal state. This would explain both the increase in the mean switching current as well as the reduction of premature switching events at lower bias currents where single thermal fluctuations could normally push the undamped phase particle over the energy barrier and down the washboard potential.

A first impression of these results may suggest that the shunted nanowire is no longer dominated by thermal behavior, unlike typical nanowire-based devices like SNSPDs. The absence of hysteresis as well as the qualitative agreement to the over-damped junction fit are both suggestive of a device that acts coherently like a Josephson junction, rather than one that supports Joule heating in its resistive domain. The observed change in the switching distribution also hints that the dynamics of the shunted device are similar to the tilted washboard approximation used to describe Josephson junctions.

Chapter 3

Switching Dynamics

Although the DC characterization of the shunted nanowire as described in Chapter 2 is suggestive of Josephson-like behavior, direct observation of the high frequency dynamics is required to gain a complete picture of the device. In this chapter, we describe the experimental setup for recording the AC voltage output of the non-hysteretic shunted nanowire, and present a simple hotspot relaxation model to explain the measured oscillations. I would like to acknowledge Qing-Yuan Zhao for his assistance in the experimental setup and measurement.

3.1 Experiment

The setup for measuring fast dynamics of the shunted nanowire is shown in Figure 3-1. As in the case of the DC measurement, the nanowire was connected to the shunt resistor using wire bonds; however, only a two-point measurement configuration was used, and series resistors were not placed in front of the PCB ports in order to avoid attenuating the high frequency voltage output. A constant bias current was supplied to the nanowire through the DC port of a bias tee (Mini Circuits, 0.1-4200 MHz) using an isolated voltage source (SIM928, Stanford Research Systems) in series with a 10 kΩ resistor. The AC output of the bias tee was sent through two low noise amplifiers (RF BAY, 0.1-2500 MHz) connected in series, leading to a total gain of 48 dB. The amplified signal was then sent to a channel of the Lecroy oscilloscope. In

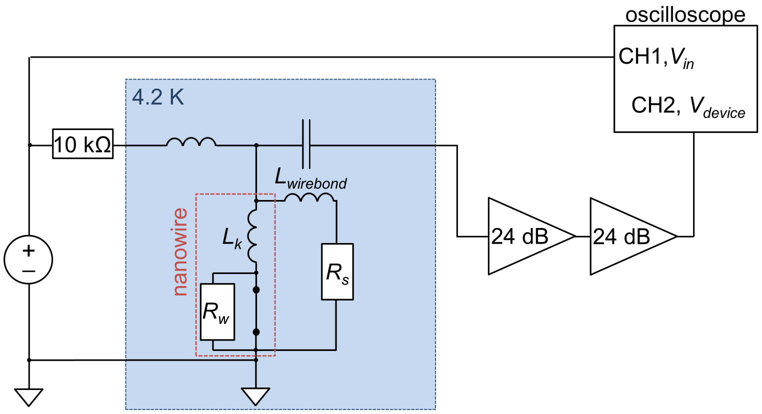

Figure 3-1: Experimental setup for measuring the high frequency voltage dynamics of the shunted nanowire.

addition to examining the raw voltage output, the frequency spectrum of the signal was captured using the Fast Fourier Transform (FFT) function of the oscilloscope. Using a custom Python script (see B.0.1), the bias current was gradually increased by ramping the voltage of the DC battery source, and both the raw waveform and the FFT spectrum were collected for each bias point.

Figure 3-2 shows the observed voltage output of the shunted nanowire when a steady bias of 40 μA was applied. As evident in the raw trace, the waveforms have a significant decay time of roughly 4.2 ns, nearly three orders of magnitude longer than a single flux quantum pulse from a Josephson junction. This was our first indication that, although the DC characteristics resemble those of a Josephson junction, the high frequency dynamics are due to a different source of nonlinear behavior.

In order to better understand these results, electrothermal simulations were performed using LTspice [39]. The electrothermal nanowire model solves for the device's dynamics by using the superconductor/normal boundary velocity to calculate the length of the resistive hotspot according to the equation [40]:

$$\frac{dl_{hs}}{dt} = v_{bound} = v_0 \frac{\Psi(I/I_c)^2 - 2}{\sqrt{\Psi(I/I_c)^2 - 1}} \tag{3.1}$$

where l_{hs} is the length of the hotspot, v_{bound} is the velocity of the superconducting boundary, v_0 is the characteristic velocity defined by the nanowire's thermal conduc-

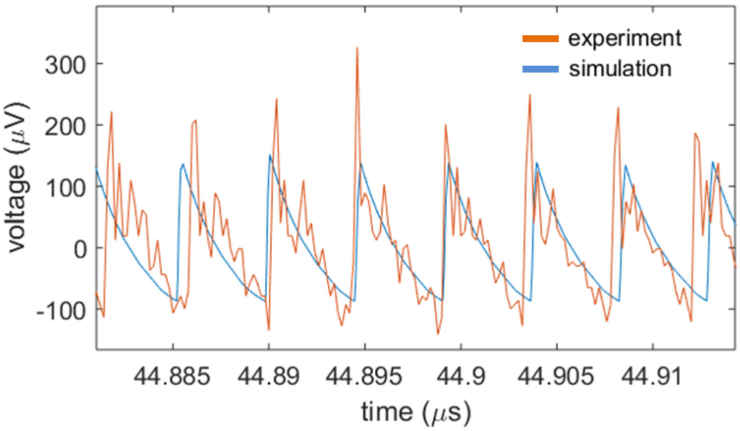

Figure 3-2: RF voltage output of a 60 nm wide nanowire (Sample B) shunted with 10 Ω when a bias current ramp is applied. The red trace corresponds to experimental data, and the blue trace is the output of the electrothermal simulations.

tivity, and Ψ is the Stekly parameter, which describes the ratio of heat generation to heat transfer. As evident by the numerator in Eq. 3.1, the velocity of the boundary and hence length of the hotspot is only increasing when $\Psi(I/I_c)^2$ is increasing, or when the bias current surpasses the critical current. For simulation purposes, a DC offset is added to the denominator in order to avoid imaginary results when the current is below I_c.

The total growing resistance of the nanowire may then be calculated based on the length of the changing hotspot according to:

$$R_n = R_S \frac{l_{hs}}{w} = R_S \frac{v_0}{w} \int \frac{\Psi(I/I_c)^2 - 2}{\sqrt{(\Psi(I/I_c)^2 - 1 + |\Psi(I/I_c)^2 - 1|)/2 + \sigma}} dt \tag{3.2}$$

where R_S is the film sheet resistance measured in Ω/square and σ is the additional parameter used to account for the DC offset. This expression can be decomposed into equivalent circuit elements by examining the related equations [39]. First we observe that the voltage through a capacitor expressed as $V = \frac{1}{C} \int i \, dt$ is in the same form as Eq. 3.2. Therefore, we can model the resistance R_n as an accumulated voltage over a capacitance defined by $(R_S \frac{v_0}{w})^{-1}$. The current through the capacitor is collectively described by the integrated terms in Eq. 3.2, and thus encapsulates the generation and transfer of heat in the nanowire. Charging or discharging of the capacitor are dictated by the simplified implementation of a current-controlled parallel switch that opens or closes based on the bias current in relation to the critical current; for instance, when the current exceeds I_c, the parallel switch opens so that the bias is diverted to the capacitor to accumulate a voltage, representing hotspot growth when the nanowire switches to the normal state. An illustration of this model and its implementation into a circuit to simulate the experimentally observed traces are shown in Figure 3-3.

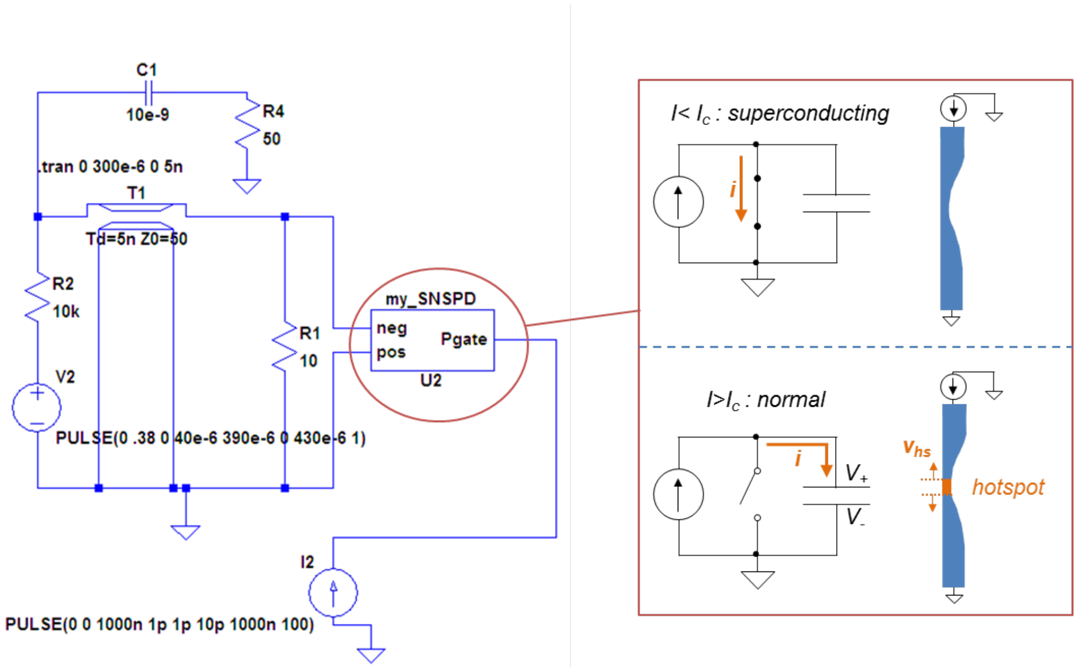

Figure 3-3: Circuit in LTspice environment for conducting electrothermal simulations of a shunted nanowire with a bias current ramp. Inset illustrates equivalent circuit model for the growing hotspot of a nanowire. When the bias is below the critical current, the switch in the circuit is closed and no voltage is accumulated on the capacitor. When the bias exceeds I_c, the switch opens and voltage builds on the capacitor, simulating the growing hotspot resistance.

The blue trace in Fig. 3-2 shows the output of the electrothermal SPICE model for a nanowire shunted by 10 Ω when the maximum hotspot resistance is set equal to 500 Ω and the inductance is set equal to 25 nH. As evident in the figure, there is good qualitative agreement between the experiment and simulation, suggesting that the observed nonlinear oscillation is caused by the interaction of a growing hotspot with the shunting circuit, rather than a type of Josephson-like behavior.

3.2 Modeling: the relaxation oscillation

Here we describe a simplified model to explain the nonlinear interaction between the hotspot and the external circuit. Figure 3-4 depicts the two time domains of a basic relaxation oscillation model from the perspective of a shunted nanowire. After the nanowire first switches into the normal state, the bias current I_{bias} is diverted to the shunt with a time constant of $\tau_1 = L/(R_s + R_w)$, where L is the inductance in series with the resistor, R_s is the shunt resistance, and R_w is the resistance of the nanowire, represented by the hotspot resistance. Once the current through the nanowire falls below the retrapping current (i_r) and allows the nanowire to return to the superconducting state, the bias is diverted back from the shunt with a time constant of $\tau_2 = L/R_s$ until the switching current (i_{sw}) is reached and the wire becomes normal again. Thus, the total period of a single relaxation oscillation may be approximated as:

$$T = -\tau_1 \ln(\frac{i_r}{i_{sw}}) - \tau_2 \ln(\frac{i_{bias} - i_{sw}}{i_{bias} - i_r}) \tag{3.3}$$

Since R_s tends to be much less than R_w, the duration set by τ_2 is expected to dominate the overall oscillation frequency, as was found in similar modeling of relaxation oscillations in hysteretic Josephson bridge contacts [41].

In the expressions for τ_1 and τ_2, the total inductance L is the sum of the nanowire's kinetic inductance L_k and the inductance of the wire bonds, L_w. However, in our experimental setup, L_w dominates the total inductance if we assume the rule of thumb that 25 μm diameter bonds have an inductance of roughly 1 nH/mm. Since typical NbN thin films (5-7 nm) have a sheet inductance of about 50 pH/sq, the maximum kinetic inductance we would expect from our nanowire geometry is less than 5 nH, given that the film used for our devices was substantially thicker. On the other hand, it is not uncommon for bonds connecting to a 10 mm x 10 mm chip to reach 5-10 mm in length, meaning that the wire bond inductance could feasibly contribute an order of magnitude more than the kinetic inductance.

Given the strong influence of wire bond inductance on the total series inductance,

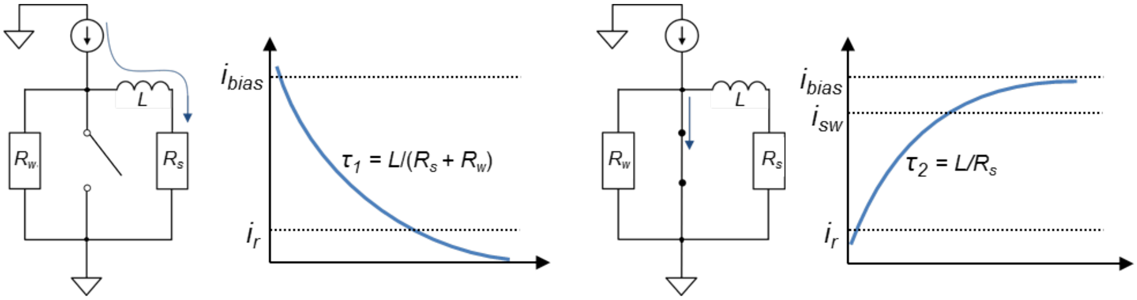

Figure 3-4: Illustration of a basic relaxation oscillation model. The bias current is first diverted to the shunt after the nanowire switches to the normal state, and then returns to the nanowire once superconductivity as been restored.

it was possible to investigate the dependence of the oscillation frequency on L by simply changing the bond length. Since the expression given in Eq. 3.3 indicates that the frequency of the oscillation is a function of both the bias current and the inductance, we experimentally investigated the impact of each of these parameters. Figure 3-5 shows our experimental data and compares the results with the model in Eq. 3.3 and with electrothermal simulations conducted in LTspice. As mentioned previously, the measurement was performed using a DC battery source in series with a 10 kΩ resistor to apply a steady bias current to the shunted device, and amplified RF voltage output was sent to the oscilloscope where its frequency spectrum was computed. The oscillation frequency was extracted from the strongest peak in the FFT using Matlab post-processing. This process was repeated for two different distances between the shunt and the nanowire, thereby changing the wire bond length and consequently the series inductance. The maximum hotspot resistance R_w was used as a fitting parameter for both the electrothermal simulation and the relaxation oscillation model, and was ultimately set equal to 500 Ω (corresponding to a length of roughly 500 nm over the 60 nm wide region). For both the model and simulation, the series inductance changed by roughly 25% between the two distances, revealing the significant impact of path inductance on the nonlinear response of the shunted system.

The results presented in Fig. 3-5 have several interesting implications. First, it is clear from the comparison of the red and black curves that the wire bond inductance greatly influences the dynamics of the shunted nanowire. This is critical from the perspective of efficient shunting, since the time delay to divert the bias current will impact how quickly the nanowire can recover the superconducting state. Additionally, although the oscillations indicate the presence of a finite hotspot, the shunting circuit allows the nanowire to be overbiased at nearly twice its critical current without latching (the point at which the nanowire becomes fully resistive). At these high bias levels, the relaxation oscillations reach a surprisingly high frequency of nearly 900 MHz. These dynamics explain the rounded shape of the shunted nanowire's current-voltage characteristics shown previously in Fig. 2-9; the rapid fluctuations are masked by the time-averaged slow measurements, but create what looks like stable voltage points along the switching portion of the curve rather than the typical abrupt transition into the resistive branch. As a result, they play a similar role to the fast Josephson oscillations in the IVC of an overdamped junction, despite their thermal nature. This also demonstrates that the absence of hysteresis in a DC current-voltage measurement is not sufficient evidence for assuming the complete absence of a hotspot—rather, it indicates that there is no sustained hotspot on the timescale at which the measurement is conducted. Therefore, high frequency measurements are crucial in gaining a complete picture of the underlying dynamics in these devices.

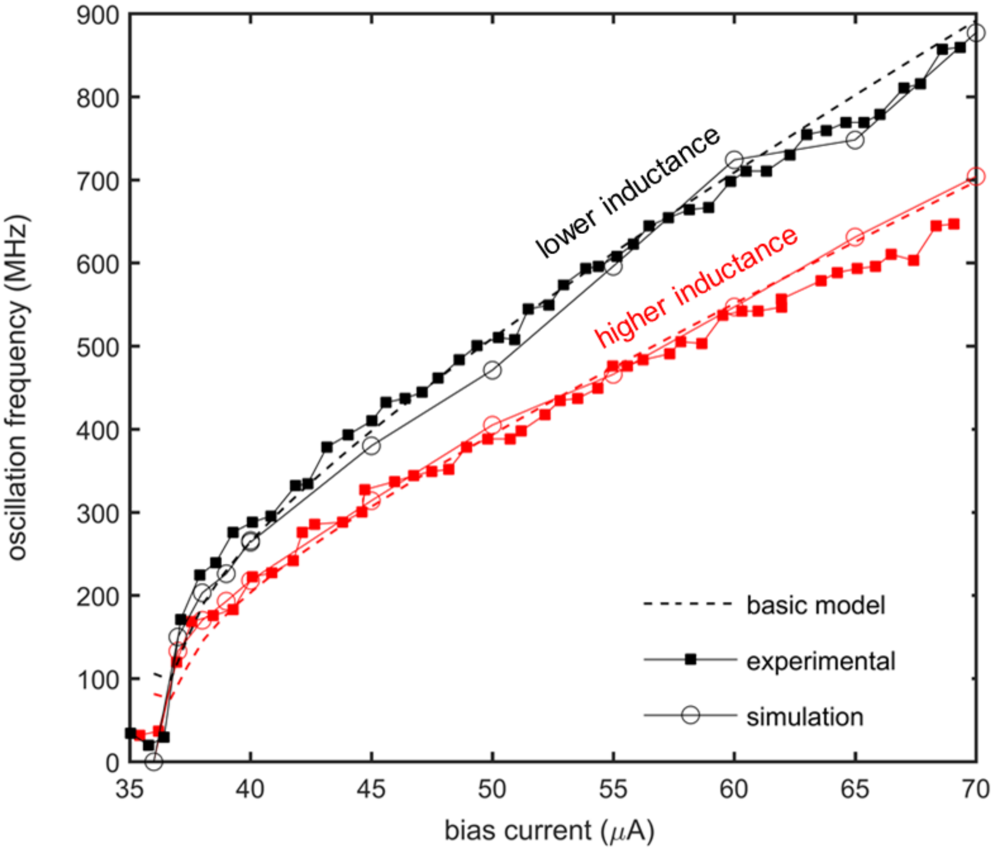

Figure 3-5: Relationship between the bias current and the oscillation frequency of Sample A shunted with 10 Ω for two different series inductances (red and black curves). The experimental data is compared to both electrothermal simulations and the basic relaxation oscillation model in Eq. 3.3. Parameters used to fit the red curve: (basic model) $L = 20$ nH, (simulation) $L = 25$ nH. Parameters used to fit the black curve: (basic model): $L = 15.3$ nH, (simulation) $L = 18.75$ nH. For all fits, $R_s = 10\ \Omega$ and $R_{wire} = 500\ \Omega$.

Chapter 4

Microwave Modulation

In Chapter 1 we described how Shapiro steps are the manifestation of phase locking between a Josephson junction's sinusoidal current-phase relationship and a periodic external drive. Although stemming from the coherent nature of a junction, the heart of this phenomenon is the synchronization of a nonlinear oscillation to a weaker periodic oscillation—a process that can be considered classical rather than inherently quantum. In this chapter we describe our experimental investigation of the effects of microwave modulation on a shunted nanowire to determine if the nonlinear interaction of the hotspot with the shunted circuit can produce similar behaviors to those normally seen in a junction. I would like to thank Di Zhu and Qing-Yuan Zhao for their helpful discussions of this chapter.

4.1 Current-voltage characteristics

Although Chapters 2 and 3 demonstrated that the time-averaged IVCs mask the direct observation of relaxation oscillations, they may provide evidence of oscillation locking under the influence of external modulation, as in the case of the AC Josephson effect. To conduct this investigation, we repeated our DC characterization measurements while subjecting the shunted nanowire to varying frequencies and powers of microwave radiation. Modulation was achieved by first soldering a wire coil to the PCB so that it hovered less than 5 mm above the sample. A high frequency sinusoidal sweep was delivered through a rigid SMA cable to the coil's port on the PCB using an RF signal generator (Stanford Research Systems, SG380).

Current-voltage characteristics were measured using the four-point scheme with the low noise preamplifier as described in Chapter 2. In order to assess whether the coupling between the coil and the nanowire was sufficient, the power to the coil was gradually increased to its maximum level at a set of frequencies ranging from 500 MHz to 4 GHz. At each of these frequencies, we could fully suppress the switching current of the nanowire if the power was increased to a critical level (dependent on the frequency), indicating that the coupling was sufficiently strong.

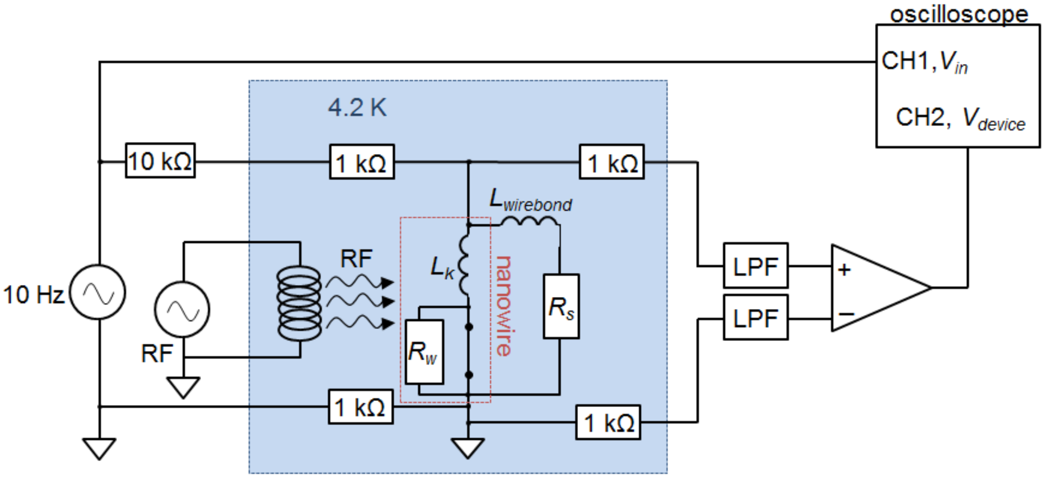

Figure 4-1: Experimental setup for measuring the DC current-voltage characteristics while subjecting the shunted nanowire to microwave radiation.

Figure 4-2 displays the current-voltage characteristics of the shunted nanowire under 180 MHz radiation. Two different power levels are shown. Increasing the power (red curve) both reduced the switching current and produced steps at voltage levels of roughly 80 μV. At 180 MHz, the anticipated Shapiro voltage ($hf/2e$) is merely 0.37 μV — less than $\frac{1}{200}$ of the voltage interval we observed experimentally. Despite this discrepancy, we also observed similarities to the AC Josephson effect in the relative amplitudes of the steps as a function of RF power. Figure 4-3 shows the amplitudes of the first four steps labeled in Fig. 4-2. Amplitudes are scaled relative to the switching current of the nanowire without applied radiation, corresponding to the initial magnitude of the first step ($v_{n_0} = 0$ μV). As evident in the figure, the

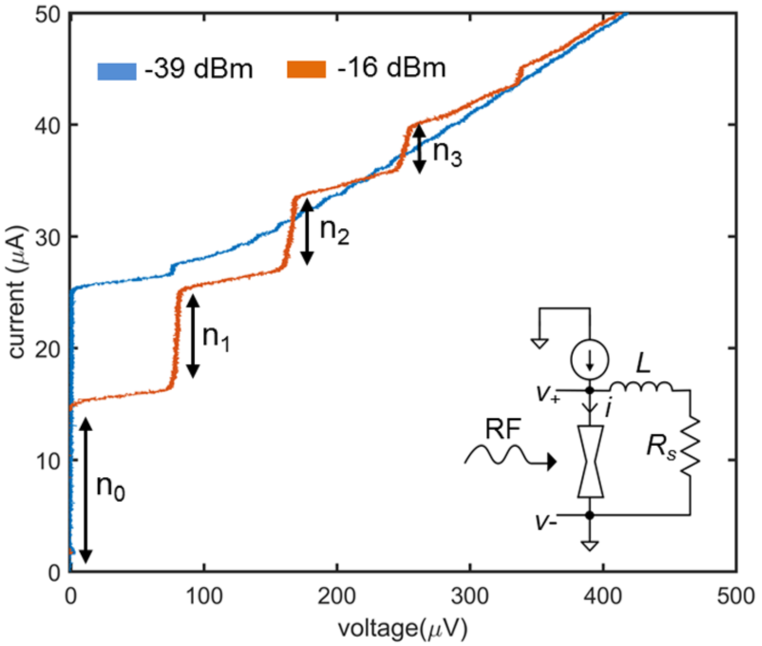

Figure 4-2: DC current-voltage characteristics of the 60 nm wide shunted nanowire (Sample B, $R_s = 10\ \Omega$) subject to 180 MHz radiation at two different powers. Inset illustrates the external radiation being applied to the nanowire during the 4-point measurement.

steps appear to have a Bessel-like relationship with the microwave power, eventually decaying to zero when the switching current was fully suppressed and the nanowire entered the normal state. This phenomenon is also present in the Shapiro effect in Josepshon junctions. Indeed, fits to the step amplitudes as a function of modulation power can be made using the Josepshon dynamical equations of Eq. 1.6, as previously done for superconducting Dayem bridges [42]. In this case, the step amplitudes follow the n^{th} order Bessel functions:

$$\frac{|I_s|}{I_c} = |J_n \frac{2e\alpha V}{hf}| \tag{4.1}$$

where V is the magnitude of the external modulation voltage and α is a fitting parameter, used here to describe the coupling loss between the coil and the nanowire in order to convert from the known power to the unknown voltage delivered to the nanowire. Using the classic conversion $P = V^2/R$, the step amplitudes can be expected to follow the Bessel relationships in Eq. 4.1 when plotted against $P^{\frac{1}{2}}$. As shown in Figure 4-3, the Bessel function fits show reasonable qualitative agreement with the experimental data. Despite the similarities to Josephson behavior, however, the IVC steps at intervals over 200 times the Shapiro voltage suggest that Josepshon-like oscillations are not the underlying mechanism observed in our nanowires. This disparity was also noted in previous work by Hadfield et al., which suggested that another type of phase locking involving relaxation oscillations may be at play [43]. As a result, the observed effect of microwaves on the DC characteristics of the shunted nanowire was our first indication that the nonlinear oscillations discussed in Chapter 3 are capable of interacting with an external periodic drive.

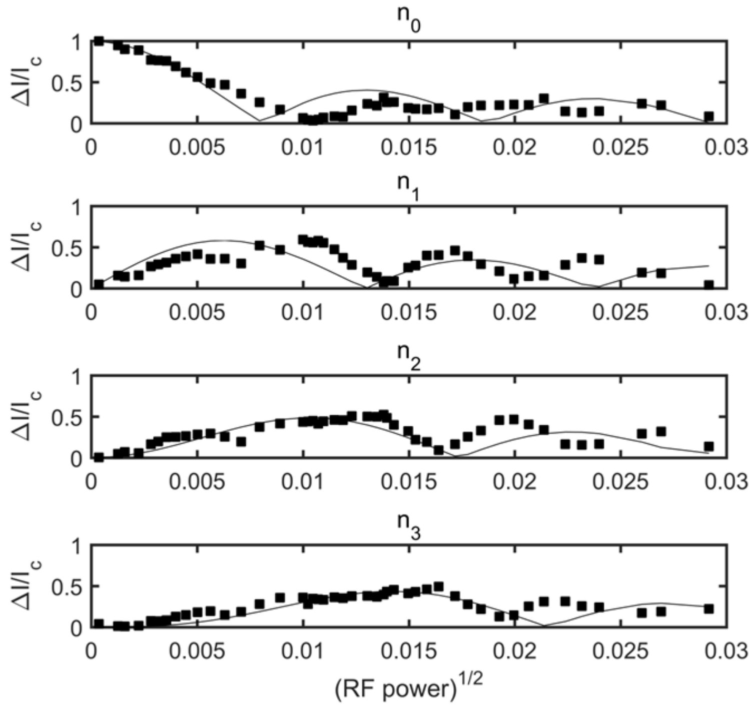

Figure 4-3: Amplitudes of the first four current steps as a function of modulation power. Amplitudes are scaled relative to I_c, the magnitude of the n_0 step when no radiation is applied. The solid black curve shows fits to dynamical solutions for a Josephson junction, following the expression $|J_n \frac{2e\alpha V}{hf}|$, where α = 1e-4.

4.2 Frequency spectrum

In Chapter 3 we discussed how the time averaged IVCs are influenced by the underlying fast oscillations which can only be observed through direct RF measurements.

Likewise, the Shapiro-like steps in the IVCs shown in Fig. 4-2 are signatures of underlying high frequency dynamics, but do not directly reveal them. Here we describe high frequency measurements to directly observe how external radiation influences the hotspot relaxation oscillations and produces Josephson-like behavior in the DC characteristics.

4.2.1 Experimental

To measure the high frequency dynamics, we again used a two-point measurement configuration without series resistors on the PCB ports. A battery source in series with a 10 kΩ resistor provided a constant bias current to the DC port of a bias tee, and the RF output was amplified using the two low noise amplifiers in series, as described in Chapter 2. The amplified voltage output was sent to the oscilloscope through an SMA cable, and its frequency spectrum was calculated using the FFT math function of the oscilloscope. The DC bias signal was also sent to the oscilloscope for averaging. A custom Python script was written to gradually sweep the bias level and record both the bias input and RF voltage output waveforms, as well as the FFT of the voltage output.

As in the case of the modulated IVC measurements, the SG380 signal generator was used to supply a high frequency sinusoidal signal to the microwave coil on the PCB. We also found we could modulate the nanowire at frequencies as low as 120 MHz, enabling use of the Agilent33600a dual channel arbitrary waveform generator for lower frequency modulation. This allowed us to ensure that the measurement was reproducible with different microwave sources.

It is important to note that the current-voltage characteristic modulation reported above and demonstrated in Fig. 4-2 was not observed for all frequencies. Rather, we found that only certain frequencies generated the Shapiro-like behavior. Since we were most interested in the underlying RF dynamics behind this behavior, we had to first identify which modulation frequencies to target.

The complete measurement process was as follows:

1. Repeat the microwave modulation of the DC current-voltage characteristics to determine which modulation frequencies generate the Shapiro-like behavior.

2. For each of those modulation frequencies, sweep the bias current and collect the raw waveforms and FFTs at each bias level.

3. Repeat the previous step at each frequency for a range of RF powers, starting with the lowest power at which no RF influence is observed and ending with the highest power before the nanowire becomes completely normal.

Since Fig. 3-5 illustrated that the natural relaxation oscillation frequency is a function of bias current, we began our analysis by examining the frequency spectrum for a single bias current at one modulation frequency and power. Figure 4-4 shows the results for the shunted nanowire biased at 60 μA under 320 MHz modulation at a power of -10 dBm. At 60 μA, the unmodulated device had a resonant frequency f_r at 504 MHz. This frequency is visible as a clear peak in the FFT of the modulated nanowire in Fig. 4-4, in addition to a peak at the drive frequency ($f_d = 320$ MHz). Peaks were also observed at mixing products of $f_r \pm m(f_d - nf_r)$, where m and n are integers. For instance, a peak at 690 MHz represents a mixing product of $n = 1$ and $m = 1$, or $2f_r - f_d$. In some cases, harmonics of the mixing products were also visible.

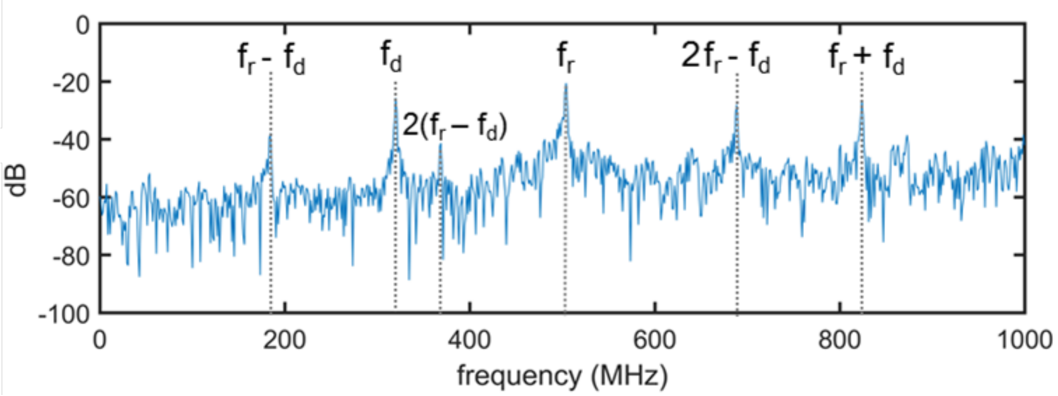

Figure 4-4: Fast Fourier transform of the shunted nanowire (Sample C, $R_s = 10\ \Omega$) voltage output with an applied radiation of 320 MHz (-10 dBm) and a constant bias current of 60 μA. Peaks indicate the resonance of the relaxation oscillations and the driving frequency, as well as their mixing products.

Comparing frequency spectrums at the same drive but varying powers revealed that, in addition to generating mixing products, the oscillation frequency was pulled towards the drive frequency as the modulation power increased. Consequently the mixing products were also seen to shift in relation to the new f_r. Figure 4-5 compares the FFTs of the shunted nanowire under 320 MHz modulation at three different powers. As the power was increased from -10 dBm to -1 dBm, the amplitude of the f_d peak increased while the resonant peak was pulled from 504 MHz to 430 MHz.

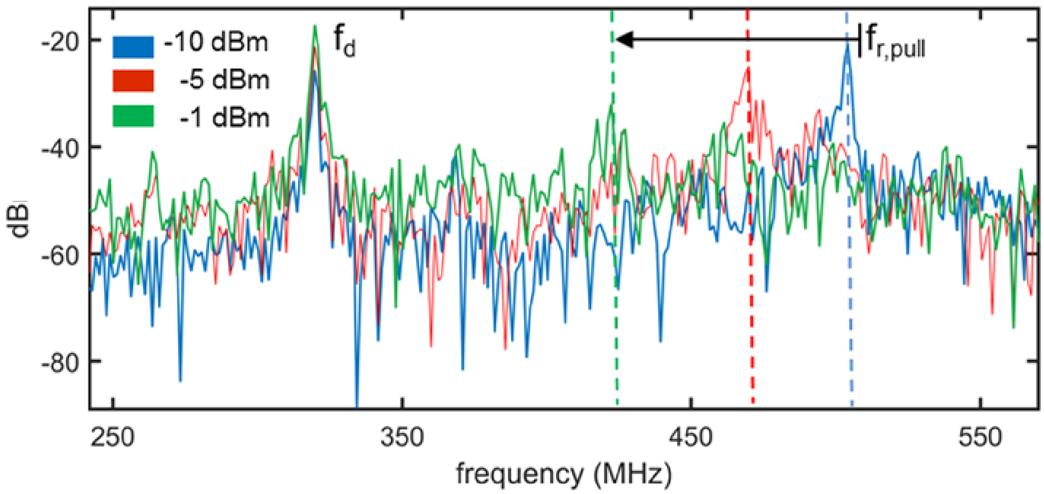

Figure 4-5: Enlarged view of the frequency spectrum (Sample C, $R_s = 10\ \Omega$) showing the drive frequency and oscillation frequency while varying the applied microwave power of a 320 MHz drive. As the power increases, the relaxation oscillation frequency is pulled down to the lower driving frequency.

We found that we could produce similar results at the same bias current at an even lower drive frequency of 120 MHz. Furthermore, this phenomena was observed at a bias condition where f_r was less than f_d, demonstrating that the oscillation frequency can be pulled in either direction. Table 4.1 summarizes these results.

Table 4.1: Pulling and mixing of frequency spectrum peaks

(a) $f_d = 320$ MHz, $I_{bias} = 60\ \mu$A

	product	-10 dBm	-5 dBm
peak 1	f_r - f_d	184	150
peak 2	f_d	320	320
peak 3	f_r	504	470
peak 4	$2f_r$-f_d	688	N/A
peak 5	f_r+f_d	824	790

(b) $f_d = 120$ MHz, $I_{bias} = 60\ \mu$A

	product	1.5 Vpp	2.5 Vpp
peak 1	f_d	120	120
peak 2	f_r-$2f_d$	266	250
peak 3	f_r-f_d	387	370
peak 4	f_r	506	490
peak 5	f_r+f_d	N/A	610

(c) $f_d = 320$ MHz , $I_{bias} = 30\ \mu$A

	product	-10 dBm	-5 dBm
peak 1	f_d-f_r	120	70
peak 2	f_r	200	250
peak 3	f_d	320	320
peak 4	$2f_d$-f_r	440	N/A
peak 5	f_d+f_r	520	570

Pulled relaxation oscillation frequencies are indicated in red font. Peaks that did not appear in the spectrum are noted as N/A. Signals listed in Table 4.1 (a) and (c) were delivered from the SG380 signal generator and have amplitudes in terms of dBm. Table 4.1 (b) used the Agilent33600a and has signal amplitudes in terms of peak-to-peak voltage. (Sample C, $R_s = 10\ \Omega$)

4.2.2 Modeling

Sawtooth model

Frequency mixing and pulling of inductively shunted tunnel junctions to a weak periodic drive have previously been explored as a means of phase locking; the strong broadband oscillations of the shunted junction were seen to mix with an injected narrowband signal, eventually producing a frequency spectrum peak at the injection frequency when the modulation power was sufficiently increased. Although the mechanism of nonlinearity in the shunted nanowire differs from that of the tunnel junction, the similarities in frequency response to an external drive make it reasonable to rely on the same basic model as presented by Calander et al.[44].

Beginning with the simplification of the relaxation oscillation as a sawtooth waveform, the current through the nanowire may be defined by:

$$I(t) = I_c \frac{t - lT^0}{T^0} \qquad for\ lT^0 \leq t \leq T^0(l+1) \tag{4.2}$$

where T^0 defines the natural period of oscillation, and l is an integer which defines the periodic waveform as a time shift from $t = 0$; for instance, the first sawtooth starting at $t = 0$ and ending at $t = T^0$ would correspond to $l = 0$, while the second sawtooth would have a linear portion defined over $T^0 \leq t \leq 2T^0$, corresponding to $l = 1$. Thus we obtain boundaries on the current through the oscillator such that

$$I(t) = 0\ for\ t = lT^0 \tag{4.3a}$$

$$I(t) = I_c\ for\ t = T^0(l+1) \tag{4.3b}$$

Applying an external drive $I_d \cos(2\pi f_d t)$ modulates the switching point of the nanowire or junction from the perspective of the supplied bias; for instance, if a signal of 3 μA is added on top of a bias at $I_c - 2\mu A$, the nanowire will exceed its critical current and switch, although the perspective of the biasing circuit will see a premature switching event at 2 μA below I_c. As a result, the new switching bias point of the circuit may be approximated as $I_{sw} = I_c + I_d \cos(2\pi f_d t)$.

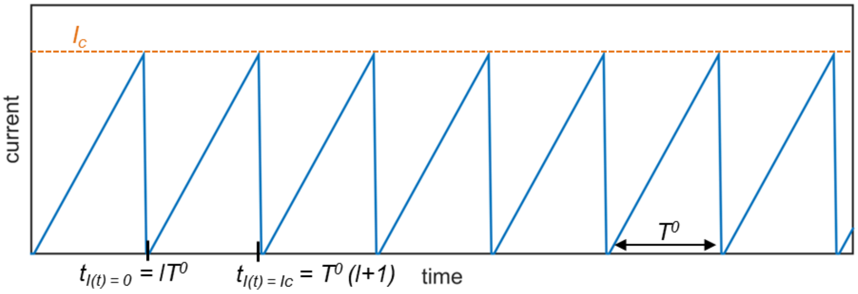

Figure 4-6: Illustration of the sawtooth relaxation oscillation model.

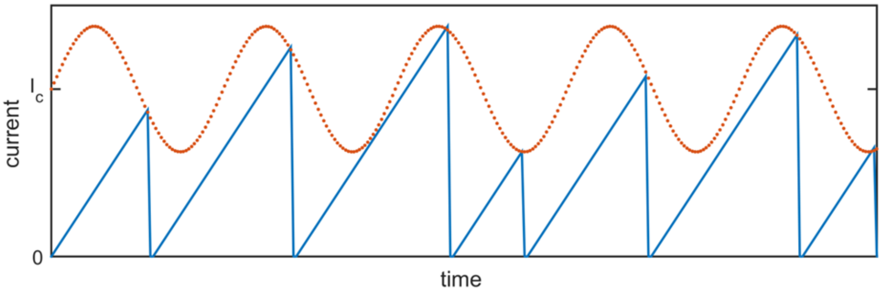

Figure 4-7: Modulation of the relaxation oscillation switching current by a sinusoidal drive.

In order to visualize how the sawtooth is locked to the external drive, it is possible to make a time transformation of $t + mT_d$, where T_d is the period of the drive and m is an integer. Since this is simply a time shift by an integer period of the drive, the value of the drive is the same before and after the transformation. Over this time shift, the current through the nanowire becomes:

$$I(t + mT_d) = I_c(t + mT_d - lT^0)/T^0 = I(t) + \frac{I_c m T_d}{T^0} \tag{4.4}$$

which implies that the current of the relaxation oscillation can be shifted to start at $I = I_c m T_d / T^0$ rather than $I = 0$, representing a new stable starting point.

As argued in [44], frequency pulling and eventual locking of the sawtooth can be understood graphically by comparing the switching points of the oscillation to the time shifted stability levels. Figure 4-8 presents two different scenarios. In Fig. 4-8(a), the sawtooth current grows towards the new switching bias point, $I_{sw} =$

$I_c + I_d \cos(2\pi f_d t)$, and then restarts at the new stable starting point $I_c m T_d / T^0$ due to the time transformation. This results in a pulling of the oscillation period towards a multiple of the drive period.

Conversely, in Fig. 4-8(b), the modulation amplitude is increased such that the switching current crosses over the new starting level. As a result, the oscillation will rise and fall with the drive period, leading to a phase lock.

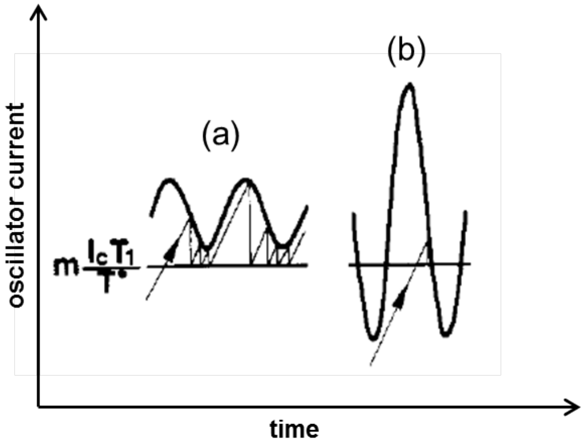

Figure 4-8: Illustration of the modulation of a sawtooth relaxation oscillation by a periodic drive. A time transformation at $t + mT_d$ is used to shift the oscillation starting level to a new stability point. (a) A weak drive will lead to frequency pulling towards mT_d without locking. (b) Increasing the drive amplitude such that it crosses the transformed starting level leads to locking of the sawtooth to the drive period. Figure adapted from [44].

Matlab simulation

In order to gain an intuitive sense of the model presented in [44], we built a simple Matlab script to simulate a relaxation oscillation modulated by a periodic drive. Building on the sawtooth equations described above, we allowed the current through the nonlinear element (representing a shunted nanowire or the inductively shunted tunnel junction) to grow as $I(t) = I_c t / T^0$ until $I_c - I(t)$ was less than an arbitrarily small number, at which point the current was reset to zero. (Note that the limit was set to be a small number rather than zero to account for discretization error). This repeated for a time vector dictated by the simulation duration and time step, producing a periodic waveform like that shown in Figure 4-6.

To incorporate the external drive, we defined a new switching current as $I_{sw} = I_c + I_d \sin(2\pi f_d t)$, where f_d and I_d were both subject to change for different simulations. Again, we allowed the current through the nonlinear element to grow as $I(t) = I_c t/T^0$; however, the switching condition was changed from $I_c - I(t) > x$ to $I_{sw} - I(t) > x$, where x is the arbitarily small number. As a result, the switching point of the sawtooth was modulated, but the slope remained unchanged. This is illustrated in Figure 4-7.

While many combinations of drive and relaxation frequencies can be simulated, we will consider two cases.

Case 1: 500 MHz oscillation with a 320 MHz drive

Figure 4-9 shows the response of a 500 MHz sawtooth to a 320 MHz modulation frequency at two different amplitudes. When the drive is at 5 μA, the FFT reveals a slight pulling of the oscillation frequency from 500 MHz to 486 MHz, as well as a mixing product of $f_r + f_d$ at 806 MHz. The pulling and mixing are both intensified when the drive is increased to 15 μA. At this drive amplitude, the oscillation frequency is pulled to 472 MHz, while mixing products of $f_r - f_d$ and $f_r + f_d$ are both present. As Table 4.2 shows, this frequency spectrum corresponds strongly to the experimentally observed results presented in Table 4.1(a) at -5 dBm.

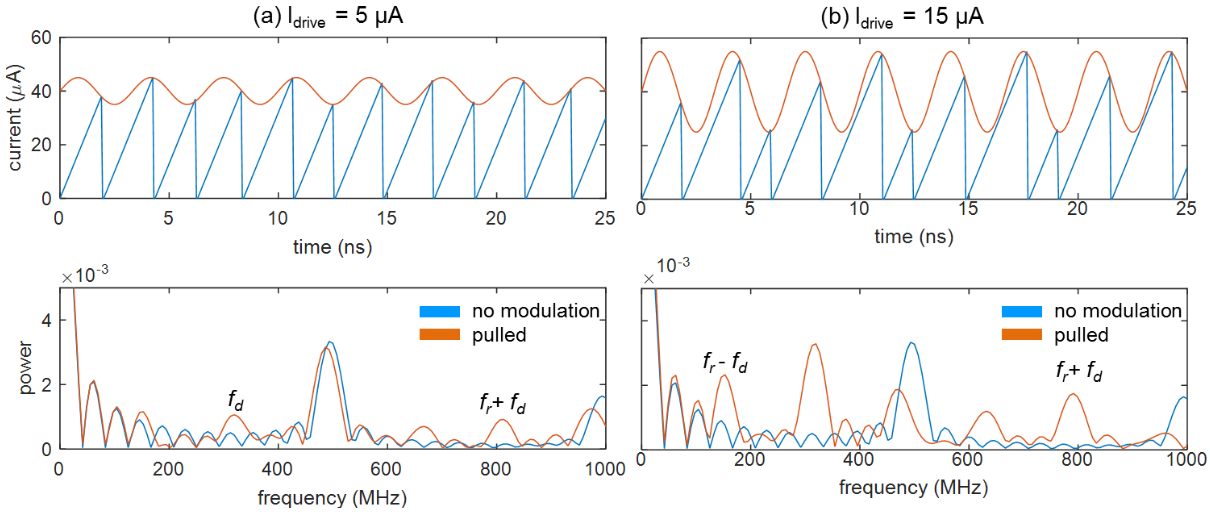

Figure 4-9: Modulation of a 500 MHz sawtooth by a 320 MHz signal. The top plots show the time domain switching behavior, and the bottom plots show the frequency spectrums. (a) $I_d = 5$ μA; (b) $I_d = 15$ μA.

Table 4.2: Model comparison of FFT peaks for 500 MHz oscillation under 320 MHz modulation

	product	experimental (-5 dBm)	model (15 μA)
peak 1	f_r - f_d	150	152.8
peak 2	f_d	320	320
peak 3	f_r	470	472.2
peak 5	f_r + f_d	790	791.7

Red text indicates the pulled frequency. For simplicity, no resonant peaks (e.g. $2f_r$) are listed, but were observed in both cases.

Case 2: 500 MHz oscillation with a 725 MHz drive

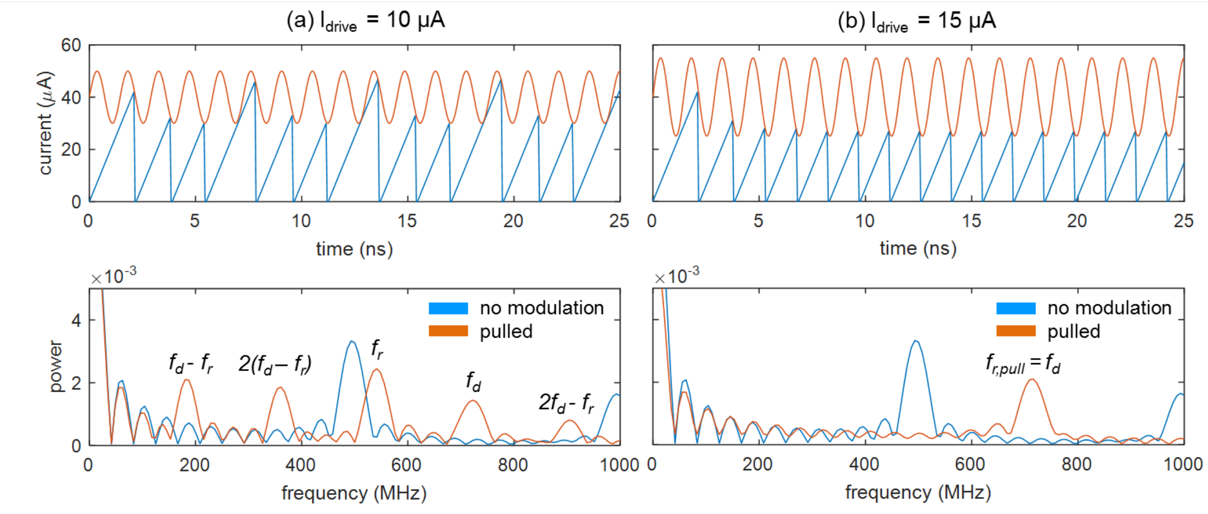

Figure 4-10: Modulation of a 500 MHz sawtooth by a 725 MHz signal. The top plots show the time domain switching behavior, and the bottom plots show the frequency spectrums. (a) $I_d = 10\ \mu$A; (b) $I_d = 15\ \mu$A.

Figure 4-10 also illustrates the modulation of a 500 MHz sawtooth, but uses a drive frequency that is higher than the natural oscillation frequency. As in the case of the 320 MHz drive, when the modulation is delivered at a lower amplitude (Fig.4-10(a)), the frequency spectrum reveals several mixing products as well as a slight pulling of the resonant frequency towards the drive. When the amplitude is further increased, however, a distinct difference is seen in both the time and frequency domains (Fig.4-

10(b))— after the first two oscillations, the sawtooth becomes fully synchronized with the modulating signal and enters the locked state. The FFT shows only a peak at the driving frequency, indicating that the relaxation oscillation is completely locked to the modulation.

Chapter 5

Conclusion and Future Work

In this thesis, we have presented a study of the nonlinear dynamics in shunted nanowires, and investigated their interaction with periodic external signals. Despite stemming from thermal rather than quantum phenomena, we find that the hotspot induced relaxation oscillations can generate similar time-averaged characteristics and microwave responses as Josephson junctions due to their fast time constants and ability to be synchronized. This understanding has several immediate implications. From the perspective of engineering a non-thermal device, the presence of relaxation oscillations in an otherwise non-hysteretic IVC emphasizes that DC characterization is not sufficient to rule out the existence of Joule heating. The observed influence of series inductance on the oscillation speed suggests that precise control of the L/R time constant is needed to eliminate hotspot formation. Additionally, the ability of relaxation oscillations to be mixed and pulled by an external drive is promising for the development of new nanowire-based devices. For example, tuning the oscillation frequency through shunt resistances or bias currents may allow for frequency multiplexing, while prior work on tunnel junctions suggests relaxation oscillations may also be used in parametric amplification [44].

These results have spurred the development of two projects that are currently underway. On one hand, we are hoping to push the limits of the relaxation oscillation frequency to the GHz range for applications such as driving SFQ pulse generators. In addition to its relatively simple fabrication, the shunted nanowire acting in the relaxation oscillation regime is appealing for its ability to be tuned by multiple parameters, a promising characteristic for various readout and detection schemes. In order to test the maximum operation frequency of the device, we are exploring questions such as how much the series inductance can be reduced before the device latches.

The most intriguing question remains the possibility of operating a superconducting nanowire in a non-thermal regime. In this work we saw that wire bonds contribute significant pathway inductance, bringing us to believe that external shunting is ultimately unsuitable for the goal of complete hotspot suppression. To avoid relaxation oscillations, we recently developed a process for lithographically shunting the nanowire with a resistor and minimal series kinetic inductance. We hope that such a design will allow for preservation of phase coherence in the nanowire during switching. Such a device would offer the advantages of Josephson-like dynamics without the fabrication or scaling difficulties.

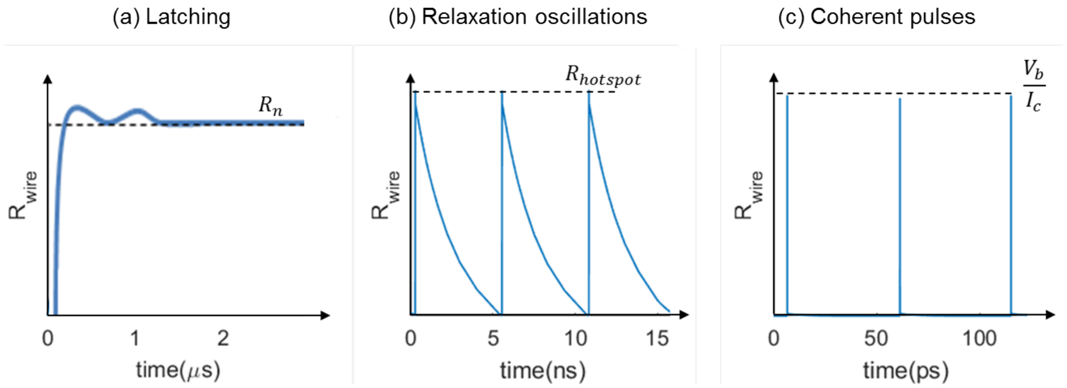

Figure 5-1: Switching regimes of a shunted superconducting nanowire, with the L/R time constant increasing from (a) to (c). In (a), the effects of shunting are negligible and the nanowire latches. (b) Shunting limits latching but does not prevent finite hotspots from forming, causing relaxation oscillations like those described in this thesis. By reducing the pathway inductance, we hope to eventually obtain state (c), in which no hotspots are formed and the nanowire acts according to phase dynamics.

Such possibilities emphasize the superconducting nanowire's importance as a platform for nonlinear investigations. Understanding the transitions between its quantum and thermal natures remains an exciting question to fundamental superconducting physics, while control of such transitions represents a powerful tool for the development of future technologies.

Appendix A

Matlab Scripts

This appendix contains Matlab scripts for simulations discussed in this thesis. Specifically, it contains code for calculating the potential energy and phase in the tilted washboard model, as well as a script for making a graphical user interface (GUI) that plots the tilted washboard potential in real time as the user changes the shunt resistance and bias current. It also contains a sample code for simulating the frequency pulling of a 506 MHz sawtooth relaxation oscillation to a 700 MHz drive.

A.0.1 Tilted washboard potential model

```
% Script to generate potential energy and phase of the tilted washboard
% particle; used in tandem with the GUI interface
function [U,phi,delta,xcoords,ycoords] = washboard(Ibias,Ic)
% note!! Ibias and Ic are in uA!!
  % Useful constants
        % constants
        e = 1.6021766208e-19; % in Coulombs
        h = 6.626070040e-34; % in Joules-s
        h_bar = h/(2*pi);
        kb = 1.38064852e-23; % Boltzmann constant
        Tc = 8; % fitting parameter for now
        eta = 4e-9; % NbN coherence length fitting parameter for now? (4 nm, from Adam's thesis)
 % Washboard parameters
 Ej = h_bar*Ic/(2*e);
 B = h_bar*Ibias/(2*e);
 % Phase evolution
phi = linspace(0,6*pi,100);
% potential
U = -Ej.*cos(phi)-B.*phi;
% calculate the energy barrier
[PKS,LOCS] = findpeaks(U);
if isempty(LOCS)
    delta = 4*sqrt(2)/2*Ej*(1-Ibias/Ic)^(3/2);
    xcoords = [];
    ycoords = [];
```

```
else
    [valley,ind] = min(U(LOCS(1):LOCS(2)));
    delta = PKS(2)-valley;
    xcoords = [phi(LOCS(2)) phi(LOCS(2))];
    ycoords = [valley PKS(2)];
end
end
```

A.0.2 GUI generator for tilted washboard model

```
% Script to generate tilted washboard GUI
function TW_knob
% initial parameters
Ibias = 12; % in microamps
Ic = 10; % in microamps
P = 1;
Rs = 100; % in ohms
% solve for initial conditions
[U,phi,delta,xcoords,ycoords] = washboard(Ibias,Ic);
% minimum potential energy
y_min = min(U);
% Create a figure and axes
    f = figure('Visible','off');
    xSize = 20; ySize = 15;
    xLeft = (50-xSize)/2; yTop = (60-ySize)/2;
        set(gcf,'PaperPosition',[xLeft yTop xSize ySize])
        set(gcf,'Position',[400 400 xSize*30 ySize*40])
 % Plot the tilted washboard
    h = plot(phi,U); xlim([min(phi) max(phi)]); ylim([
       y_min 1e-14]);
    if ~isempty(xcoords)
        line(xcoords,ycoords,'Color','r')
    end
   % Create slider
    sld1 = uicontrol('Style', 'slider',...
        'Min',1,'Max',2*Ic,'Value',1,...
        'Position', [400 22 120 22],...
        'Callback', @TWpower);
```

```
%        Create slider
    sld2 = uicontrol('Style', 'slider',...
        'Min',10,'Max',500,'Value',500,...
        'Position', [100 22 120 22],...
        'Callback', @TWpower);
 % Add a text uicontrol to label the slider.
    txt = uicontrol('Style','text',...
        'Position',[50 15 120 15],...
        'String','10');
  % Add a text uicontrol to label the slider.
    txt = uicontrol('Style','text',...
        'Position',[150 15 120 15],...
        'String','500');
    % Add a text uicontrol to label the slider.
    txt = uicontrol('Style','text','FontSize',12 ,...
        'Position',[20 20 80 20],...
        'String','R');
% Add a text uicontrol to label the slider.
    txt = uicontrol('Style','text','FontSize',12 ,...
        'Position',[270 20 120 20],...
        'String','Ibias');
 % Add a text uicontrol to label the slider.
    txt = uicontrol('Style','text',...
        'Position',[350 15 120 15],...
        'String','1 uA');
  % Add a text uicontrol to label the slider.
    txt = uicontrol('Style','text',...
        'Position',[450 15 120 15],...
        'String','2 Ic');
% Make figure visble after adding all components
```

```
    f.Visible = 'on';
    function TWpower(source,callbackdata)
        val1 = sld1.Value; % bias
        val2 = sld2.Value; % resistance
        [U,phi,delta,xcoords,ycoords] = washboard(val1,Ic)
           ;
            h = plot(phi,U); xlim([min(phi) max(phi)]);
               ylim([y_min 1e-14])
              if ~isempty(xcoords)
                 line(xcoords,ycoords,'Color','r')
             end
            title(sprintf('Energy Barrier = %.3g\n',delta)
               ,'Color','r')
            TW_test(val1,Ic,val2)
    end
end

% reference: http://www.mathworks.com/help/matlab/ref/
   uicontrol.html
```

A.0.3 Simulation of modulated sawtooth

```
% Script to illustrate frequency pulling in a sawtooth
   waveform
% Example: 506 MHz sawtooth with 700 MHz sinusoidal drive
% ----- Parameters-------------------------------------%
% Triangular waveform
I = 0;
Ic = 40e-6; % critical current in Amps
Itot = [I];
T = 1/(506e6);  % period of the relaxation oscillations
tstep = 50e-12;
tmax = 25e-9;
time = linspace(0,tmax,501);
t = 0;
while length(Itot)< (tmax/tstep)+1
    if Ic-I > .1e-6 % limit to assess whether I(t) has
       reached Ic
         I = Ic*(t)/T;
         t = t+tstep;
    else
        I = 0;
        t = 0;
    end
    Itot = [Itot I];
end
%------ PLOT UNMODULATED RESULTS
   -------------------------------------%
figure(1); subplot(2,1,1);plot(1e9*time,1e6*Itot); title('
   unmodulated sawtooth')
```

```
xlabel('time (ns)'); ylabel('current (\muA)')
% ------- SINUSOIDAL DRIVE
   ----------------------------------%
% add sinusoidal drive
I_drive = 33e-6;
Ic_new = Ic + I_drive.*sin(2*pi*700e6*time);
% Repeat simulation except with added sinusoidal drive
I = 0;
Itot_pull = [];
Ic_new_tot = [];
t = 0;
i = 1;
while length(Itot_pull)< (tmax/tstep)+1
    ICN = Ic_new(i);
    if ICN-I > .1e-6
         I = Ic*(t)/T;
         t = t+tstep;
    else
        I = 0;
        t = 0;
    end
    Itot_pull = [Itot_pull I];
    Ic_new_tot = [Ic_new_tot ICN];
    i = i+1;
end
%------ PLOT MODULATED RESULTS
   ----------------------------------%
figure(1);
subplot(2,1,2);plot(1e9*time,1e6*Itot_pull);set(gca,'
   FontSize',11); hold on;
```

```
plot(1e9*time,1e6*Ic_new_tot); set(gca,'FontSize',11);
   xlabel('time (ns)'); ylabel('current (\muA)')
title('modulated sawtooth')
legend('oscillation','periodic drive')
```

Appendix B

Python measurement code

B.0.1 Code to measure oscillation frequency during a bias sweep

```
# Emily Toomey, 2/06/17
# Code for measuring the relaxation oscillations of a
   nanowire as a function of bias current


# ----------IMPORT USEFUL FUNCTIONS
   -------------------------------%
from standard_measurements.ic_sweep import *
from standard_measurements.iv_sweep import *
from useful_functions.save_data_vs_param import *
import numpy as np
import time
import scipy.io as sio
import visa
import datetime
```

```
#---------- IMPORT DEVICES
   -----------------------------------------$
from instruments.srs_sim928 import SIM928
SRS = SIM928("GPIB0::2::INSTR",8) # second number is the
   port name of the device
# setup oscilloscope
from instruments.lecroy_620zi import LeCroy620Zi
lecroy = LeCroy620Zi("TCPIP::qnn-scope2.mit.edu::INSTR")

# Print all available GPIB resources
visa.ResourceManager().list_resources()

# import waveform generator
from instruments.agilent_33250a import Agilent33250a
awg = Agilent33250a('GPIB0::11::INSTR')


#------- DEFINE THE FUNCTIONS AND CHANNELS
   --------------------------------------------
# Channel Labels
lecroy.label_channel('C1', 'Input')
lecroy.label_channel('C3', 'V_device')

lecroy.set_math('F1','FFT','C3')
lecroy.view_channel('F1')
lecroy.set_parameter('P1','Mean','C1', show_table = True)


# ----------SET UP VOLTAGES
   ---------------------------------------------------
```

```
# SRS VOLTAGES
voltages = np.linspace(350,950,80)
FFT = []
FREQ = []
VIN = []
T2 = []
VOUT = []
n = 0
sample_name = 'NWL051I_A4A_10_ohms_noRF_'
SRS.set_output(True)
for v in voltages:
        SRS.set_voltage(v/1000)
        t2,C2 = lecroy.get_wf_data('C3')
        Vin = lecroy.get_parameter_value('P1')
        tf,Ft = lecroy.get_wf_data('F1')
        FFT.append(Ft)
        FREQ.append(tf)
        VIN.append(Vin)
        T2.append(t2)
        VOUT.append(C2)
        print 'voltage number = %.3f ' % v
        n = n +1
        time.sleep(0.3)
        # SAVE DATA

data = {'FFT':FFT,'FREQ':FREQ,'VIN':VIN,'T2':T2,'VOUT':
   VOUT}
myfilename = 'NWL051I_A4A_10_ohms_noRF_'
myfilename_data = path_name+myfilename  + '.mat'
myfilename_pic = path_name +myfilename + '.png'
```

```
myfilename_screenshot = path_name +myfilename +'screenshot'+ '.png'

lecroy.save_screenshot(myfilename_screenshot)



sio.savemat(myfilename_data, data)
SRS.set_voltage(0)
SRS.set_output(False)
```

Bibliography

[1] B. v. d. P. D.Sc and J. van der Mark, “LXXII. The heartbeat considered as a relaxation oscillation, and an electrical model of the heart,” *The London, Edinburgh, and Dublin Philosophical Magazine and Journal of Science*, vol. 6, pp. 763–775, Nov. 1928.

[2] J. E. Rose, J. F. Brugge, D. J. Anderson, and J. E. Hind, “Phase-locked response to low-frequency tones in single auditory nerve fibers of the squirrel monkey.,” *Journal of Neurophysiology*, vol. 30, pp. 769–793, July 1967.

[3] S. Varigonda and T. T. Georgiou, “Dynamics of relay relaxation oscillators,” *IEEE Transactions on Automatic Control*, vol. 46, pp. 65–77, Jan. 2001.

[4] R. Lang and K. Kobayashi, “Suppression of the relaxation oscillation in the modulated output of semiconductor lasers,” *IEEE Journal of Quantum Electronics*, vol. 12, pp. 194–199, Mar. 1976.

[5] C. J. R. H, “Keyboard oscillator circuit,” Nov. 1966. U.S. Classification 84/672, 327/113, 984/380, 327/569; International Classification G10H5/00, G10H5/04; Cooperative Classification G10H5/04; European Classification G10H5/04.

[6] W. E. Kock, “Electrical generation of musical tones,” Dec. 1938. U.S. Classification 84/692, 331/174, 984/384, 331/49, 331/130, 331/128, 315/245, 84/DIG.130, 315/239, 315/242; International Classification G10H5/10; Cooperative Classification Y10S84/13, G10H5/10; European Classification G10H5/10.

[7] J. Shutt, “Dual mode relaxation oscillator generating a clock signal operating at a frequency substantially same in both first and second power modes,” Feb. 2006. U.S. Classification 331/143, 713/320, 331/111; International Classification G06F1/00, H03K3/26, H03K3/02; Cooperative Classification H03K3/0231, G06F1/04, G06F1/32; European Classification G06F1/04, H03K3/0231, G06F1/32.

[8] O. H. S. Jr, “Multi-mode relaxation oscillator,” Feb. 1981. U.S. Classification 331/65, 331/111, 331/143, 340/521; International Classification H03K3/0231, G08B17/10, G08B23/00; Cooperative Classification G08B23/00, H03K3/0231, G08B17/10; European Classification H03K3/0231, G08B17/10, G08B23/00.

[9] K. Choe, O. D. Bernal, D. Nuttman, and M. Je, “A precision relaxation oscillator with a self-clocked offset-cancellation scheme for implantable biomedical SoCs,” in *2009 IEEE International Solid-State Circuits Conference - Digest of Technical Papers*, pp. 402–403,403a, Feb. 2009.

[10] W. S. Snyder and D. V. Ess, “Capacitance sensor using relaxation oscillators,” Dec. 2007. U.S. Classification 331/150, 324/548, 324/678, 324/658; International Classification H03K3/02, G01R27/26; Cooperative Classification H03K5/26, H03K3/0231, G01R27/2605; European Classification G01R27/26B, H03K5/26, H03K3/0231.

[11] B. D. Josephson, “Possible new effects in superconductive tunnelling,” *Physics Letters*, vol. 1, pp. 251–253, July 1962.

[12] P. L. Richards, “Chapter 6 The Josephson Junction as a Detector of Microwave and Far-Infrared Radiation,” *Semiconductors and Semimetals*, vol. 12, pp. 395–440, Jan. 1977.

[13] M. T. Levinsen, R. Y. Chiao, M. J. Feldman, and B. A. Tucker, “An inverse ac Josephson effect voltage standard,” *Applied Physics Letters*, vol. 31, pp. 776–778, Dec. 1977.

[14] C. Granata, A. Vettoliere, and M. Russo, “Integrated dc SQUID Magnetometers in Multichannel Systems for Biomagnetic Imaging,” in *EUROCON 2007 - The International Conference on "Computer as a Tool"*, pp. 556–563, Sept. 2007.

[15] S. Shapiro, A. R. Janus, and S. Holly, “Effect of Microwaves on Josephson Currents in Superconducting Tunneling,” *Reviews of Modern Physics*, vol. 36, pp. 223–225, Jan. 1964.

[16] T. P. Orlando and K. A. Delin, *Foundations of Applied Superconductivity*. Addison-Wesley, 1991. Google-Books-ID: 7yRRAAAAMAAJ.

[17] G. N. Gol’tsman, O. Okunev, G. Chulkova, A. Lipatov, A. Semenov, K. Smirnov, B. Voronov, A. Dzardanov, C. Williams, and R. Sobolewski, “Picosecond superconducting single-photon optical detector,” *Applied Physics Letters*, vol. 79, pp. 705–707, Aug. 2001.

[18] A. N. McCaughan and K. K. Berggren, “A Superconducting-Nanowire Three-Terminal Electrothermal Device,” *Nano Letters*, vol. 14, pp. 5748–5753, Oct. 2014.

[19] A. N. McCaughan, N. S. Abebe, Q.-Y. Zhao, and K. K. Berggren, “Using Geometry To Sense Current,” *Nano Letters*, vol. 16, pp. 7626–7631, Dec. 2016.

[20] H. L. Hortensius, E. F. C. Driessen, T. M. Klapwijk, K. K. Berggren, and J. R. Clem, “Critical-current reduction in thin superconducting wires due to current crowding,” *Applied Physics Letters*, vol. 100, p. 182602, Apr. 2012.

[21] Q.-Y. Zhao, A. N. McCaughan, A. E. Dane, K. K. Berggren, and T. Ortlepp, "A nanocryotron comparator can connect single-flux-quantum circuits to conventional electronics," *Superconductor Science and Technology*, vol. 30, no. 4, p. 044002, 2017.

[22] A. J. Kerman, E. A. Dauler, W. E. Keicher, J. K. W. Yang, K. K. Berggren, G. Gol'tsman, and B. Voronov, "Kinetic-inductance-limited reset time of superconducting nanowire photon counters," *Applied Physics Letters*, vol. 88, p. 111116, Mar. 2006.

[23] K. S. Il'in, M. Lindgren, M. Currie, A. D. Semenov, G. N. Gol'tsman, R. Sobolewski, S. I. Cherednichenko, and E. M. Gershenzon, "Picosecond hot-electron energy relaxation in NbN superconducting photodetectors," *Applied Physics Letters*, vol. 76, pp. 2752–2754, May 2000.

[24] M. Beck, M. Klammer, S. Lang, P. Leiderer, V. V. Kabanov, G. N. Gol'tsman, and J. Demsar, "Energy-Gap Dynamics of Superconducting NbN Thin Films Studied by Time-Resolved Terahertz Spectroscopy," *Physical Review Letters*, vol. 107, p. 177007, Oct. 2011.

[25] K. K. Likharev and V. K. Semenov, "RSFQ Logic/Memory Family: A New Josephson-Junction Technology for Sub-Terehertz-Clock-Frequency Digital Systems," *IEEE Transactions on Applied Superconductivity*, vol. 50, no. 1, 1991.

[26] W. Chen, A. V. Rylyakov, V. Patel, J. E. Lukens, and K. K. Likharev, "Rapid single flux quantum T-flip flop operating up to 770 GHz," *IEEE Transactions on Applied Superconductivity*, vol. 9, pp. 3212–3215, June 1999.

[27] W. J. Skocpol, M. R. Beasley, and M. Tinkham, "Self-heating hotspots in superconducting thin-film microbridges," *Journal of Applied Physics*, vol. 45, pp. 4054–4066, Sept. 1974.

[28] M. Tinkham, J. U. Free, C. N. Lau, and N. Markovic, "Hysteretic I-V curves of superconducting nanowires," *Physical Review B*, vol. 68, p. 134515, Oct. 2003.

[29] N. Kumar, C. B. Winkelmann, S. Biswas, H. Courtois, and A. K. Gupta, "Controlling hysteresis in superconducting constrictions with a resistive shunt," *Superconductor Science and Technology*, vol. 28, no. 7, p. 072003, 2015.

[30] M. W. Brenner, D. Roy, N. Shah, and A. Bezryadin, "Dynamics of superconducting nanowires shunted with an external resistor," *Physical Review B*, vol. 85, p. 224507, June 2012.

[31] S.-Z. Lin and D. Roy, "Role of kinetic inductance in transport properties of shunted superconducting nanowires," *Journal of Physics: Condensed Matter*, vol. 25, no. 32, p. 325701, 2013.

[32] A. J. Kerman, D. Rosenberg, R. J. Molnar, and E. A. Dauler, “Readout of superconducting nanowire single-photon detectors at high count rates,” *Journal of Applied Physics*, vol. 113, p. 144511, Apr. 2013.

[33] A. E. Dane, *Reactive DC Magnetron Sputtering of Ultrathin Superconducting Niobium Nitride Films.* PhD thesis, Massachusetts Institute of Technology, 2015.

[34] J. K. W. Yang, E. Dauler, A. Ferri, A. Pearlman, A. Verevkin, G. Gol’tsman, B. Voronov, R. Sobolewski, W. E. Keicher, and K. K. Berggren, “Fabrication development for nanowire GHz-counting-rate single-photon detectors,” *IEEE Transactions on Applied Superconductivity*, vol. 15, pp. 626–630, June 2005.

[35] J. Zmuidzinas, “Superconducting Microresonators: Physics and Applications,” *Annueal Review of Condensed Matter Physics*, vol. 3, pp. 169–214, Feb. 2012.

[36] P. Dubos, P. Charlet, T. Crozes, P. Paniez, and B. Pannetier, “Thermostable trilayer resist for niobium lift-off,” *Journal of Vacuum Science & Technology B: Microelectronics and Nanometer Structures Processing, Measurement, and Phenomena*, vol. 18, pp. 122–126, Jan. 2000.

[37] A. E. Grigorescu and C. W. Hagen, “Resists for sub-20-nm electron beam lithography with a focus on HSQ: State of the art,” *Nanotechnology*, vol. 20, no. 29, p. 292001, 2009.

[38] A. G. Caster, S. Kowarik, A. M. Schwartzberg, O. Nicolet, S.-H. Lim, and S. R. Leone, “Observing hydrogen silsesquioxane cross-linking with broadband CARS,” *Journal of Raman Spectroscopy*, vol. 40, pp. 770–774, July 2009.

[39] Q.-Y. Zhao, “Electrical Modeling of Superconducting Nanowire Devices,” Nov. 2016.

[40] A. J. Kerman, J. K. W. Yang, R. J. Molnar, E. A. Dauler, and K. K. Berggren, “Electrothermal feedback in superconducting nanowire single-photon detectors,” *Physical Review B*, vol. 79, p. 100509, Mar. 2009.

[41] M. Mück, H. Rogalla, and C. Heiden, “Relaxation oscillators made of bridge-type Josephson contacts,” *Applied Physics A*, vol. 46, pp. 97–101, June 1988.

[42] P. E. Gregers-Hansen, M. T. Levinsen, L. Pedersen, and C. J. Sjøstrøm, “Variation with microwave power of the current steps of superconducting microbridges,” *Solid State Communications*, vol. 9, pp. 661–664, May 1971.

[43] R. H. Hadfield, A. J. Miller, S. W. Nam, R. L. Kautz, and R. E. Schwall, “Low-frequency phase locking in high-inductance superconducting nanowires,” *Applied Physics Letters*, vol. 87, p. 203505, Nov. 2005.

[44] N. Calander, T. Claeson, and S. Rudner, “Relaxation Oscillations in Inductively Shunted Josephson Tunnel Junctions,” *Physica Scripta*, vol. 25, no. 6A, p. 837, 1982.